

Award Number: W81XWH-09-1-0191

TITLE: Development of an MRI-Guided Intra-Prostatic Needle Placement System

PRINCIPAL INVESTIGATOR: Gregory S. Fischer

CONTRACTING ORGANIZATION: Worcester Polytechnic Institute  
Worcester, MA 01609

REPORT DATE: July 2011

TYPE OF REPORT: Annual

PREPARED FOR: U.S. Army Medical Research and Materiel Command  
Fort Detrick, Maryland 21702-5012

DISTRIBUTION STATEMENT: Approved for Public Release;  
Distribution Unlimited

The views, opinions and/or findings contained in this report are those of the author(s) and should not be construed as an official Department of the Army position, policy or decision unless so designated by other documentation.

<b>REPORT DOCUMENTATION PAGE</b>			<i>Form Approved</i> <i>OMB No. 0704-0188</i>		
Public reporting burden for this collection of information is estimated to average 1 hour per response, including the time for reviewing instructions, searching existing data sources, gathering and maintaining the data needed, and completing and reviewing this collection of information. Send comments regarding this burden estimate or any other aspect of this collection of information, including suggestions for reducing this burden to Department of Defense, Washington Headquarters Services, Directorate for Information Operations and Reports (0704-0188), 1215 Jefferson Davis Highway, Suite 1204, Arlington, VA 22202-4302. Respondents should be aware that notwithstanding any other provision of law, no person shall be subject to any penalty for failing to comply with a collection of information if it does not display a currently valid OMB control number. <b>PLEASE DO NOT RETURN YOUR FORM TO THE ABOVE ADDRESS.</b>					
<b>1. REPORT DATE</b> July 2011		<b>2. REPORT TYPE</b> Annual		<b>3. DATES COVERED</b> 1 July 2010 – 30 June 2011	
<b>4. TITLE AND SUBTITLE</b>  Development of an MRI-Guided Intra-Prostatic Needle Placement System			<b>5a. CONTRACT NUMBER</b>		
			<b>5b. GRANT NUMBER</b> W81XWH-09-1-0191		
			<b>5c. PROGRAM ELEMENT NUMBER</b>		
<b>6. AUTHOR(S)</b>  Gregory Fischer  E-Mail: <a href="mailto:gfischer@wpi.edu">gfischer@wpi.edu</a>			<b>5d. PROJECT NUMBER</b>		
			<b>5e. TASK NUMBER</b>		
			<b>5f. WORK UNIT NUMBER</b>		
<b>7. PERFORMING ORGANIZATION NAME(S) AND ADDRESS(ES)</b>  Worcester Polytechnic Institute Worcester, MA 01609			<b>8. PERFORMING ORGANIZATION REPORT NUMBER</b>		
<b>9. SPONSORING / MONITORING AGENCY NAME(S) AND ADDRESS(ES)</b> U.S. Army Medical Research and Materiel Command Fort Detrick, Maryland 21702-5012			<b>10. SPONSOR/MONITOR'S ACRONYM(S)</b>		
			<b>11. SPONSOR/MONITOR'S REPORT NUMBER(S)</b>		
<b>12. DISTRIBUTION / AVAILABILITY STATEMENT</b> Approved for Public Release; Distribution Unlimited					
<b>13. SUPPLEMENTARY NOTES</b>					
<b>14. ABSTRACT</b>  Magnetic Resonance Imaging (MRI) is an ideal interventional guidance modality: it provides near real-time high-resolution images at arbitrary orientations and is able to monitor therapeutic agents, surgical tools, biomechanical tissue properties, and physiological function. MRI poses formidable engineering challenges by severely limited access to the patient and high magnetic field that prevents the use of conventional materials and electronic equipment. The objective is to make conventional diagnostic closed high-field MRI scanners available for guiding prostatic needle placement interventions using a robotic assistant. In Year 2 we defined system workflow and developed an integrated hardware and software system consists of a navigation software, a robot middleware interface, a piezoelectric motor controller and a 6 degree of freedom (DOF) needle placement robot with integrated fiberoptic force sensing. We have validated the system workflow, MRI compatibility and needle steering capability with real-time MRI guidance.					
<b>15. SUBJECT TERMS</b> Image-guided diagnosis & therapy, MRI, haptics & telesurgery, Robotics					
<b>16. SECURITY CLASSIFICATION OF:</b>			<b>17. LIMITATION OF ABSTRACT</b>	<b>18. NUMBER OF PAGES</b>	<b>19a. NAME OF RESPONSIBLE PERSON</b> USAMRMC
<b>a. REPORT</b> U	<b>b. ABSTRACT</b> U	<b>c. THIS PAGE</b> U			<b>19b. TELEPHONE NUMBER</b> (include area code)
			UU	60	

## Table of Contents

	<u>Page</u>
Introduction.....	4
Body.....	5
Key Research Accomplishments.....	5
Reportable Outcomes.....	13
Conclusion.....	13
References.....	14
Appendices.....	16

## **INTRODUCTION:**

Magnetic Resonance Imaging (MRI) is an excellent imaging modality for many conditions, but to date there has been limited success in harnessing this modality for the guidance of interventional procedures. MRI is an ideal interventional guidance modality: it provides near real-time high-resolution images at arbitrary orientations and is able to monitor therapeutic agents, surgical tools, biomechanical tissue properties, and physiological function. At the same time, MRI poses formidable engineering challenges by severely limited access to the patient and high magnetic field that prevents the use of conventional materials and electronic equipment. Currently, no technological solution exists to assist MRI guided prostate interventions in an accurate, simple, and economical manner. The objective of our research is to make conventional diagnostic closed high-field MRI scanners available for guiding prostatic needle placement interventions. Our approach is to employ robotic assistant devices for assisting clinicians with needle placement while taking advantage of real time MR images for guidance. In this work, we apply a remotely actuated robotic needle placement system in standard closed high-field magnets, optimized for transperineal prostate biopsy and brachytherapy seed placement.

## **BODY:**

Please see the publications included in the appendix for a detailed account of the published work to date. Specific accomplishments in Year 2 by aim of the research plan are detailed below.

### **Aim 1: Refined Requirements and System Design**

In Year 1, we worked closely with our collaborators at the Brigham and Women's Hospital and Johns Hopkins University to refine the requirements of the robotic system [Song 2010]. The most critical parameters relevant to design of the robotic assistant are related to patient positioning and placement of the robot.

In Year 2 we focused on the workflow. To satisfy the design requirements of interventional needle placement robot we proposed a system workflow that mimics traditional transrectal ultrasound (TRUS) guided prostate needle insertions to maximally retain surgical workflow that physicians are comfortable with. This workflow as shown in Fig. 1 below includes five states of operation and follows a coherent procedure.

- **Initialization.** The hardware and software system is initialized. In this state, the operator prepares the robot by connecting the robot controller, applying sterile drape, attaching sterile needle contacting components, and inserting the needle. The robot is calibrated to a pre-defined home position and loads the robot configuration from XML file.
- **Planning.** Pre-operative MR images are loaded into the 3D Slicer and the target locations are selected in patient/image RAS coordinates.
- **Calibration.** A series of transverse images of a fiducial frame on the robot are acquired. Multiple images are used to perform multi-slice registration to enhance system accuracy. This registration step enables conversion between image coordinates to robot coordinates.
- **Targeting.** Needle target is selected from the Slicer software and this desired position is transmitted to the robot interface software module to process inverse kinematics and the calculated joint command is used to drive piezoelectric motors. Targets may also be directly entered or adjusted in the robot proxy interface. Real-time MR images can be acquired during insertion that enable visualization of the tool path.
- **Verification.** The robot forward kinematics calculates actual needle tip position (from encoder measurements and registration results) which is displayed in the 3D Slicer. Post insertion MR images are acquired and displayed with overlaid target and actual robot position.

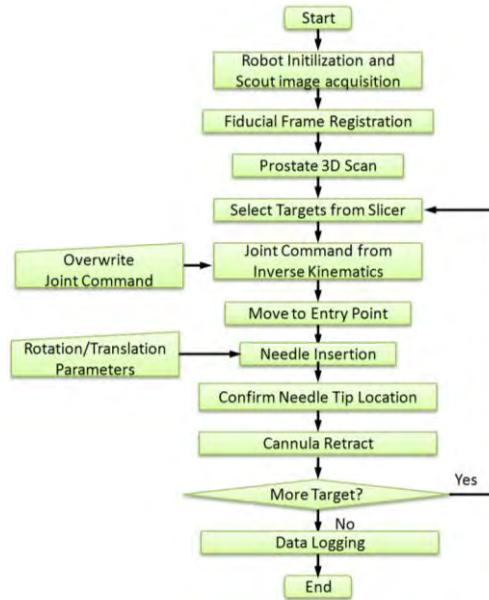


Figure 1 - Workflow of MRI-guided needle placement that mimics that of traditional TRUS-guided prostate needle intervention

## Aim 2: Advanced Needle Driver Development

### Actuation

In Year 1 we developed a prototype piezoelectric actuation system. By leveraging our previous effort on piezoelectric actuation and motor driver development, in Year 2 we further refined the piezoelectric driver design as shown in Fig. 2 [Cole 2001, Cole 2011, Fischer 2011]. There are many shapes and forms of piezoelectric actuators, and they generally fall into two major categories: harmonic and non-harmonic. While non-harmonic motors, operate at a much lower frequency than harmonic motors (750Hz to 3kHz) they require a high precision non-sinusoidal waveform to be operated most effectively. Although we have focused on PiezoMotor nonharmonic actuators, we have shown our drive system to operate with all popular commercially available piezo actuators. The signal processing stage receives an input in the form of a velocity or position set point. This signal processing block can then create four independent channels of driving waveforms with a data rate of 12.5 mega samples per second of 14 bit resolution. The signal generators include a high power output amplification stage, which passes its signals out to the actuators through a  $\pi$  filter. The boards also integrate position encoding (from differential encoder receivers) such that closed-loop motion control loops can take place within the FPGA, distributing the real-time processing of the system. Fig. 2 shows the latest board design and the backplane configuration that goes inside the controller enclosure containing five piezoelectric driver boards.

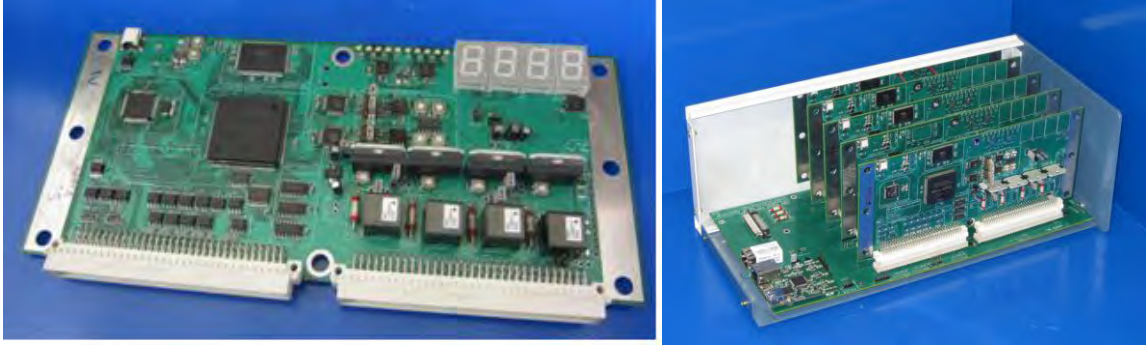


Figure 2 – Latest iteration (Rev. C) of the piezoelectric actuator driver architecture. This custom drive circuit provides four FPGA-based waveform synthesizers and corresponding amplifiers that read motor-specific waveforms from an SD card(left). Multiple driver boards can be utilized on a single backplane for easy connection to the robot and enables communication through a single fiber optic Ethernet connection (right).

Sensing

Sensing is required to implement a teleoperation framework with force feedback [Su 2011c]. In Year 1 we developed a 3 DOF fiber optic force/torque sensor for measuring tissue-needle interactions [Su 2009, Su 2010]. In Year 2, we further designed a Fabry-Perot interferometry (FPI) based miniaturized force sensor. Even though fiber optic sensors are generally accredited for better survivability in hazardous environments, meticulous design considerations are still required to build robust and durable sensors. For intra-body applications, sensor miniaturization and tool integrability are essential for surgical procedures. In particular, for prostate interventions, the sensor should be small in size and easy to integrate with surgical needle.

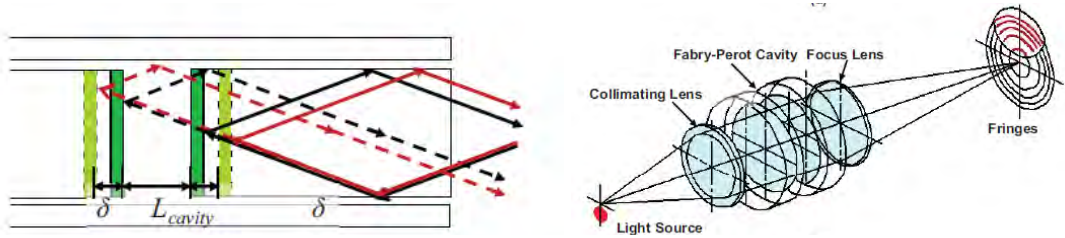


Figure 3 - Fabry-Perot sensing principle: light propagation in Fabry-Perot cavity (left) and resulting fringe pattern (right).

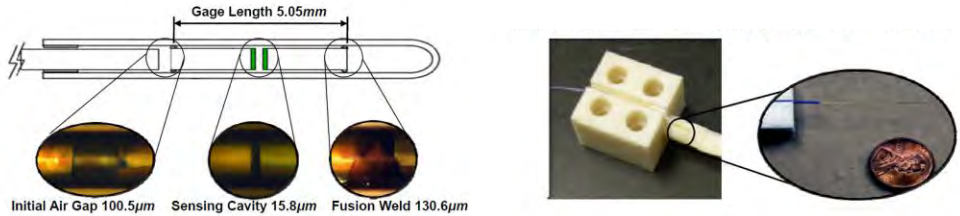


Figure 4 - Magnified fiber FPI strain sensor with three segment dimensions (left) and FPI embedded in an ABS cantilever beam and the inset shows the fiber with a cent (right).

Besides immune to electromagnetic and RF signal and substantially cheaper than fiber Bragg grating sensor, the advantages of FPI sensor includes: 1) static/dynamic response capability, 2) high sensitivity and resolution, 3) no interference due to cable bending and 4) robust to a large range of temperature variation ( $-40^{\circ}\sim 250^{\circ}$ ) due to air gap insulation to the sensing region. As shown in Fig. 3 & 4, the main component of the FPI is the sensing cavity, measuring  $15.8\mu\text{m}$  wide. A glass capillary covering the sensing region is fusion welded to the fiber in two locations and encapsulates the sensor. There is an air gap of approximately  $100.5\mu\text{m}$  wide. The total length of the FPI sensor, including the glass capillary, and bare fiber is approximately  $20\text{mm}$ .

Fig. 5 (top) shows the configuration of the custom-made FPI sensor interface and sensor location on the robot needle driver [Su 2011d]. Due to negligible friction force between the needle and needle guide, the reaction forces between the mechanism (top plate) and the actuator drive rod is used to measure needle insertion force as shown in the Fig. 5 (bottom-right). The beam to hold the actuator rod has a small  $1:59\text{mm}$  groove to lay the sensor that would extend  $30\text{mm}$  along its side where the FPI sensor could be embedded.  $10\text{ Newton}$  interaction force is the maximum required for each sensor. The finite element analysis illustrates the maximum strain  $100\mu\epsilon$  under  $10\text{ Newton}$  axial force using ABS plastic material. Calibration results are shown in Fig. 5 (bottom-left).

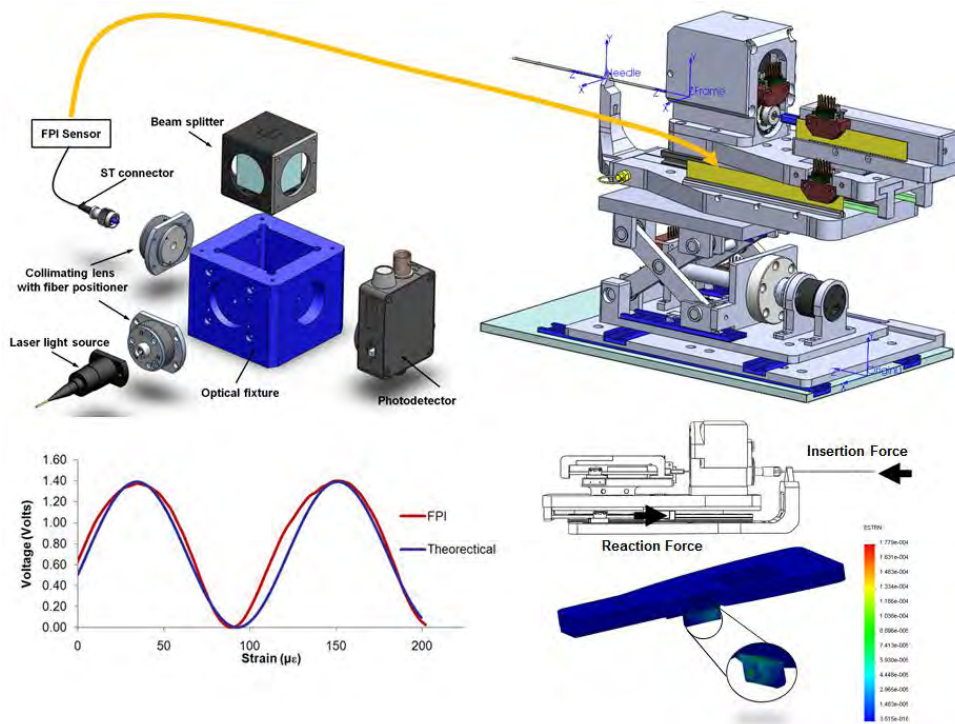


Figure 5 - Fabry-Perot interferometry-based force sensing of needle insertion force. Intended configuration (top), calibration of a test fixture (bottom-left) and FEM of the needle driver to predict deflection under typical  $10\text{N}$  insertion force.



## Needle Manipulation

We have developed the first prototype of a MRI-compatible piezoelectric actuated robot integrated with a high-resolution fiber optic sensor for prostate brachytherapy with real-time in situ needle steering capability in 3T MRI [Su 2011c]. The 6 DOF robot consists of a modular 3 DOF needle driver with fiducial tracking frame and a 3 DOF actuated Cartesian stage. The needle driver provides needle cannula rotation and translation (2 DOF) and stylet translation (1 DOF). The driver mimics the manual physician gesture by two point grasping (stylet and cannula). The robot design is shown in Fig. 6.

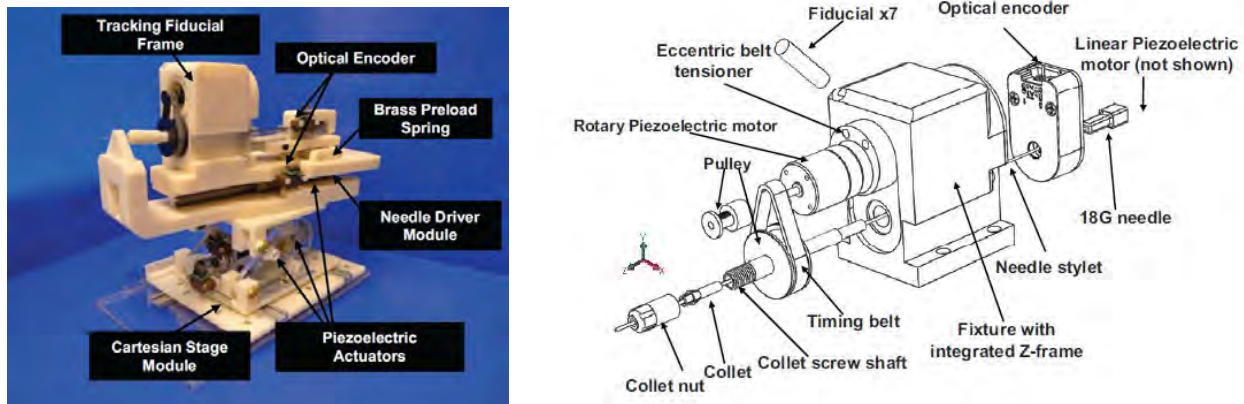


Figure 6 - Physical prototype of 6-DOF piezoelectric actuated needle placement robot (left). An exploded view of the needle clamping mechanism, fiducial frame and motor fixture (right).

### Aim 3: Robotic System Integration

We have developed an integrated system consisting of four major components: Navigation software, robot interface software and communication protocols, robot controller, and the robot itself [Su 2011a]. Three-dimensional surgical navigation software 3D Slicer serves as a user interface to visualize planning MRI images and define targets in image/patient RAS coordinates. We have developed a robot interface software that relies upon OpenIGTLink, a network protocol designed to work on the TCP/IP application layer to handle transform, image and device control. Communication from the robot interface to the robot controller is through a fiber optic Ethernet connection run through the patch panel wave guide, as this eliminates a large source of noise that is introduced when electrical signals are passed through the walls of the scanner room.

Fig. 7 shows the system architecture – Slicer is used to select the target position in MR images, the target is transmitted through OpenIGTLink to the robot interface software, registration results and inverse kinematics are used to determine the appropriate robot configuration, the commands are sent to the robot controller, and the controller actuates the piezoelectric motors under precise closed loop control. For verification, the tip position is calculated based on the robot forward kinematics and registration results to overlay the actual needle location (as determined from robot encoders) on the MR images in Slicer.

The complete robotic system has been tested in a 3T MRI scanner during in phantom trials. The robot shown in Fig. 8 (left) resides on the scanner bed and operates within the bore of the scanner without any noticeable MR image degradation. The robot is connected via a single shielded electrical cable to the robot controller which sits in the scanner room beside the bed as shown in Fig. 8 (right).

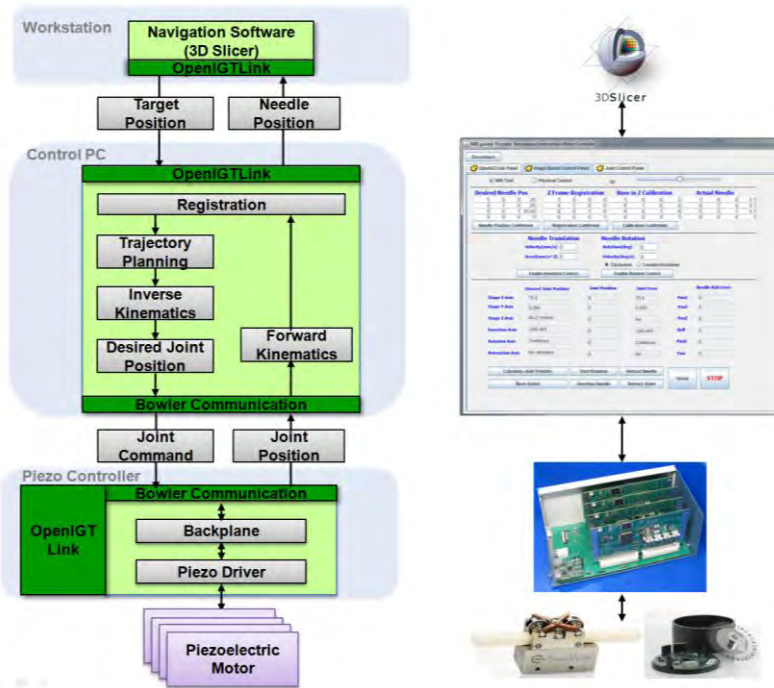


Figure 7 - System architecture: system architecture diagram shows the connection and data flow. OpenIGTLink is used to exchange control, position, and image data (left). The corresponding components (right).

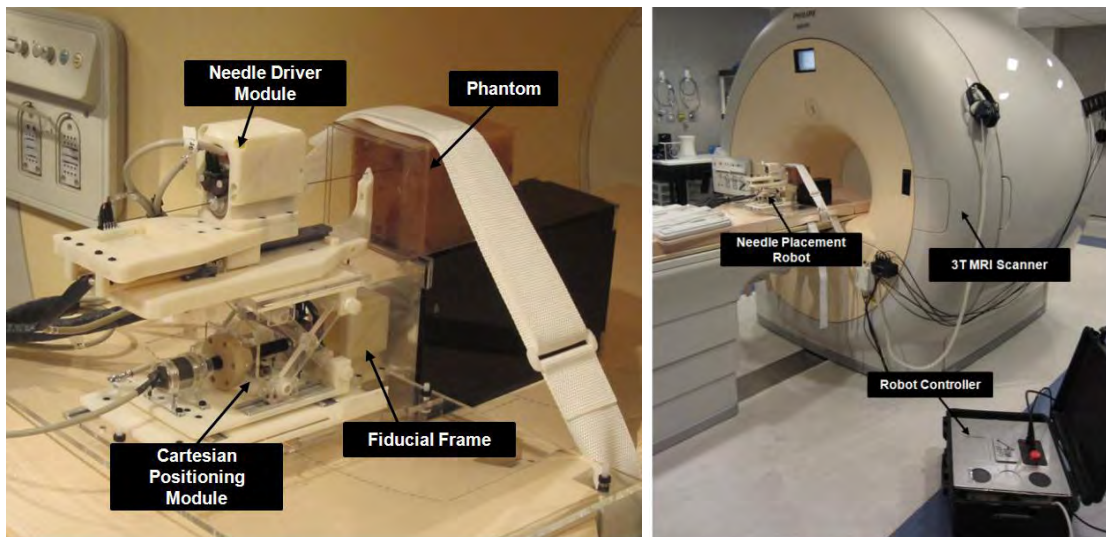
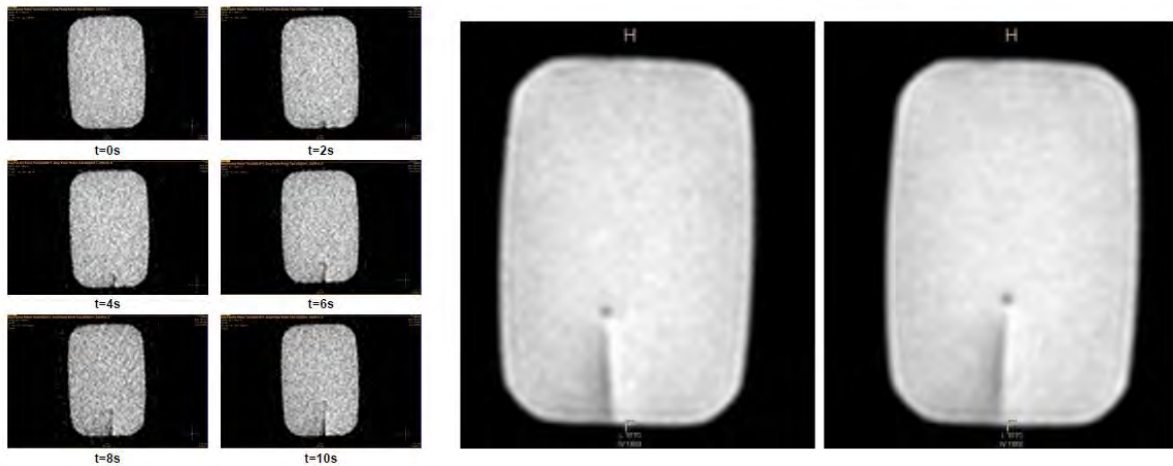


Figure 8 - A detailed view of the robot with phantom inside MRI (left). The prototype needle placement robot for percutaneous prostate interventions inside 3T MRI scanner and the robot controller is inside the scanner room beside the scanner (right).

#### Aim 4: Validation

MRI compatibility of the initial prototype was evaluated in Year 1. We have continued to confirm compatibility of the latest controller design, and found that even during simultaneous robot motion and imaging, no more than 5% SNR loss is found. Therefore, we are confident in the ability of the current system to operate during imaging with no noticeable image quality degradation.

With the fully functional system, a series of experiments are performed to evaluate the system performance for needle insertion and steering capability under real-time 3T MRI-guidance [Su 2011c]. The first test is the dynamic needle insertion. Ballistics gelatin is utilized as a tissue phantom for evaluating needle insertion. This imaging protocol provides 2.5Hz update rates. Needle insertion precisely controlled by the robot controller during simultaneous imaging. Fig. 9 (left) depicts six needle insertion snapshots during 3T echo-planar imaging at 0.4 second interval. The needle shaft and tip trajectories are clearly visualized in the phantom image without major interference during robot motion.



*Figure 9 - Needle insertion snapshots during real-time 3T echo-planar imaging at 0.4 second interval (left) and Bevel tip needle steering image in 3T MRI (right).*

In the second test, the same 22 Gauge medical needle is used to demonstrate compensation of the needle path by controlled bevel-tip steering with MRI visualization. The bevel tip is rotated toward left before insertion. T2-weighted fast spin echo (field of view 240mm, echo time 90ms, repetition time 3000ms, flip angle 90°) illustrates the final needle shape and tip position. The same procedure is repeated for bevel right before insertion and the results are shown in Fig. 9 (right). There is no visually identifiable interference during needle robot controlled insertion.

To determine the systems effectiveness at controlling actuators, it was designed to drive a PiezoLEGS rotary motor that was coupled to a US Digital, 1250 count quadrature optical encoder, and then driven through a series of step response and sine response experiments. These experiments were structured such that a position set point was supplied to the driver on a timed schedule, and the encoder information was read and recorded in real time as shown in the figure below. These results shown in Fig. 9 demonstrate the ability of the controller system to drive an actuator with finer precision than a single encoder tick, which in this case corresponds to a 0.072

degree or change. Similar results or encoder-level accuracy were found with the linear motors which are measured using a 1000 cpi quadrature encoder, thus an accuracy of 0.006mm. Note that the purpose of this study was to measure the inherent accuracy of the robot actuators, the limiting factor in the clinical system is the pixel size of the selected MRI scan protocol and the corresponding registration accuracy (typically sub-pixel). Phantom studies are run with 0.5mm pixel size.

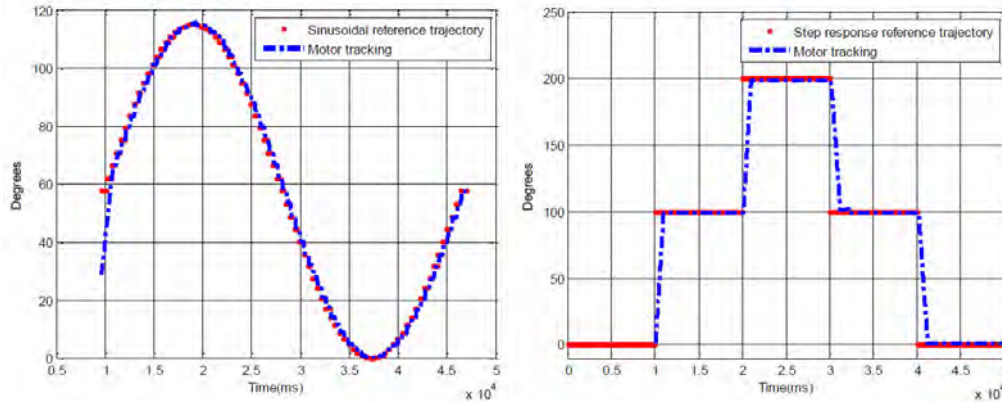


Figure 10 - Motor position (blue) and set point (red) plotted against time for two trials: dynamic sinusoid motion (left) and step response (right).

## **KEY RESEARCH ACCOMPLISHMENTS:**

- Defined system workflow
- Developed next generation, clinically viable control system
- Developed an integrated networked hardware and software system to support the proposed surgical workflow
- Refined 6 DOF needle placement robot including 3 DOF needle driver module
- Developed a miniaturized Fabry-Perot interferometry based fiberoptic force sensor
- Demonstrated a fully functionally robot inside 3T MRI scanner
- Validated capability of needle placement under real-time MR imaging
- Evaluated robotic system accuracy

## **REPORTABLE OUTCOMES:**

Please see References section for publications resulting from this research.

## **CONCLUSION:**

Based on the requirements defined in Year 1, we defined a surgical workflow and developed an integrated hardware and software system that consists of a refined 6 DOF needle placement robot with fiber optic force sensing utilizing a miniaturized Fabry-Perot interferometry sensor, a software controller with Ethernet communication, and an improved piezoelectric motor controller. With ex vivo phantom study, we have integrated the system and evaluated system workflow, MRI compatibility, image registration accuracy and robot tracking accuracy. In the coming year, we will enhance system accuracy and reliability, complete bilateral teleoperation with fiberoptic sensor based force feedback. The final deliverable at the end of the project period will be a teleoperated version of the robot shown that is tested in phantom studies in preparation for pre-clinical trials at BWH.

## REFERENCES:

- [Cole 2010] Cole G, Harrington K, Su H, Camilo A, Pilitsis J, Fischer GS, Closed-Loop Actuated Surgical System Utilizing Real-Time In-Situ MRI Guidance, 12th International Symposium on Experimental Robotics – ISER 2010, Dec 2010.
- [Cole 2011] Cole G, Harrington K, Su H, Camilo A, Pilitsis J, Fischer GS, Closed-Loop Actuated Surgical System Utilizing Real-Time In-Situ MRI Guidance, Springer Tracts in Advanced Robotics, eds. O. Khatib, V. Kumar, G. Sukhatme, Springer-Verlag, 2011.
- [Fischer 2011] Fischer GS, Cole A, Su H, Approaches to Creating and Controlling Motion in MRI, In Proceedings of the 33rd Annual International Conference of the IEEE Engineering in Medicine and Biology Society (EMBC), Boston, USA, 2011 (Invited Paper)
- [Song 2010] Song S, Cho NB, Fischer GS, Hata N, Tempany C, Fichtinger G, Iordachita I, Development of a Pneumatic Robot for MRI-guided Transperineal Prostate Biopsy and Brachytherapy: New Approaches, International Conference on Robotics and Automation - ICRA, May 2010.
- [Su 2009] Su H, Fischer GS, A 3-Axis Optical Force/Torque Sensor for Prostate Needle Placement in Magnetic Resonance Imaging Environments, 2nd Annual IEEE International Conference on Technologies for Practical Robot Applications - TePRA 2009, Woburn, Massachusetts, November 2009.
- [Su 2010] Su H, Shang W, Cole GA, Harrington K, Fischer GS, Haptic System Design for MRI-Guided Needle Based Prostate Brachytherapy, Haptics Symposium - Haptics 2010, Waltham, Massachusetts, March 2010.
- [Su 2011a] Su H, Cole G, Hata N, Tempany C, Fischer GS, Real-time MRI-Guided Transperineal Needle Placement Prostate Interventions with Piezoelectrically Actuated Robotic Assistance, Radiological Society of North America 97th Scientific Assembly and Annual Meeting, Chicago, USA, 2011. (accepted)
- [Su 2011b] Su H., Camilo A., Cole G.A., Hata N., Tempany C, Fischer GS, High-Field MRI-Compatible Needle Placement Robot for Prostate Interventions. Stud Health Technol Inform, pp 623-629, 2011.
- [Su 2011c] Su H., Zervas M., Cole G., Furlong C., Fischer GS, Real-time MRI-guided Needle Placement Robot with Integrated Fiber Optic Force Sensing, IEEE ICRA 2011 International Conference on Robotics and Automation. Shanghai, China, 2011.
- [Su 2011d] Su H., Zervas M., Furlong C., Fischer GS, A Miniature MRI-compatible Fiber-Optic Force Sensor Utilizing Fabry-Perot Interferometer, MEMS and Nanotechnology, Conference Proceedings of the Society for Experimental Mechanics Series, pp. 131-136, 2011.
- [Su 2011e] Su H, Iordachita I, Yan X, Cole G, Fischer GS, Reconfigurable MRI-Guided Robotic Surgical Manipulator: Prostate Brachytherapy and Neurosurgery Applications, In

Proceedings of the 33rd Annual International Conference of the IEEE Engineering in Medicine and Biology Society (EMBC), Boston, USA, 2011.

- [Su 2011f] H. Su and G. S. Fischer, “High-field MRI-Compatible Needle Placement Robots for Prostate Interventions: Pneumatic and Piezoelectric Approaches”, eds. T. Gulrez and A. Hassanien, *Advances in Robotics and Virtual Reality*, Springer-Verlag, 2011. (In Press)
- [Tokuda 2009] Tokuda J, Fischer GS, Papademetris X, Yaniv Z, Ibanez L, Cheng P, Liu H, Blevins J, Arata J, Golby A, Kapur T, Pieper S, Burdette E, Fichtinger G, Tempany C, Hata N, *OpenIGTLink: An Open Network Protocol for Image-Guided Therapy Environment*, *Int Jnl Medical Robotics & Computer Assisted Surgery*, vol. 5, no. 4, pp. 423-34, July 2009.
- [Tokuda 2010] Tokuda J, Fischer GS, DiMaio SP, Gobbi DG, Csoma C, Mewes PW, Fichtinger G, Tempany CM, Hata N, *Integrated Navigation and Control Software System for MRI-guided Robotic Prostate Interventions*, *Computerized Medical Imaging and Graphics*, vol. 34, no. 1, pp. 3-8, Jan 2010.
- [Wang 2009] Wang Y, Cole G, Su H, Pilitsis JG, Fischer GS, *MRI Compatibility Evaluation of a Piezoelectric Actuator System for a Neural Interventional Robot*, EMBC, Sept 2009.
- [Wang 2010] Wang Y, Su H, Harrington K, Fischer GS, *Sliding mode control of piezoelectric valve regulated pneumatic actuator for MRI-compatible robotic intervention*, ASME Dyn Sys and Controls Conf (DSCC), Sept 2010.
- [Wang 2010] Wang Y, Su H, Harrington K, Fischer GS, *Sliding mode Control of Piezoelectric Valve Regulated Pneumatic Actuator for MRI-Compatible Robotic Intervention*, ASME Dynamic Systems and Control Conference - DSCC 2010, Cambridge, Massachusetts, September 2010.

## **APPENDICES:**

Su H., Zervas M., Cole G., Furlong C., Fischer GS, Real-time MRI-guided Needle Placement Robot with Integrated Fiber Optic Force Sensing, IEEE ICRA 2011 International Conference on Robotics and Automation. Shanghai, China, 2011.

*This publication was presented at ICRA 2011 and represents the most recent published work from the proposed research plan.*

Su H, Cole GA, Fischer GS, High-field MRI-Compatible Needle Placement Robots for Prostate Interventions: Pneumatic and Piezoelectric Approaches, To appear in: Advances in Robotics and Virtual Reality, Published by Springer in the Intelligent Systems Reference Library Series.

*This accepted book chapter presents our experience in developing MRI-compatible robotic devices and a comparison of actuation approaches. The piezoelectrically actuated MRI-compatible robot for percutaneous prostate surgery is the focus of the proposed system.*

Cole G, Harrington K, Su H, Camilo A, Pilitsis J, Fischer GS, Closed-Loop Actuated Surgical System Utilizing Real-Time In-Situ MRI Guidance, To appear in: Experimental Robotics, Published by Springer in Tracts in Advanced Robotics.

*This publication presents the development of the modular MRI-compatible robot controller and system architecture that is used by the prototype and will be the basis of the control system used for the proposed robotic system.*

*Additional publications available on request.*



# Real-time MRI-Guided Needle Placement Robot with Integrated Fiber Optic Force Sensing

Hao Su, Michael Zervas, Gregory A. Cole, Cosme Furlong, Gregory S. Fischer

**Abstract**—This paper presents the first prototype of a magnetic resonance imaging (MRI) compatible piezoelectric actuated robot integrated with a high-resolution fiber optic sensor for prostate brachytherapy with real-time *in situ* needle steering capability in 3T MRI. The 6-degrees-of-freedom (DOF) robot consists of a modular 3-DOF needle driver with fiducial tracking frame and a 3-DOF actuated Cartesian stage. The needle driver provides needle cannula rotation and translation (2-DOF) and stylet translation (1-DOF). The driver mimics the manual physician gesture by two point grasping. To render proprioception associated with prostate interventions, a Fabry-Perot interferometer based fiber optic strain sensor is designed to provide high-resolution axial needle insertion force measurement and is robust to large range of temperature variation. The paper explains the robot mechanism, controller design, optical modeling and opto-mechanical design of the force sensor. MRI compatibility of the robot is evaluated under 3T MRI using standard prostate imaging sequences and average signal noise ratio (SNR) loss is limited to 2% during actuator motion. A dynamic needle insertion is performed and bevel tip needle steering capability is demonstrated under continuous real-time MRI guidance, both with no visually identifiable interference during robot motion. Fiber optic sensor calibration validates the theoretical modeling with satisfactory sensing range and resolution for prostate intervention.

**Keywords:** Optical Force Sensor, Fabry-Perot Interferometer, MRI Compatibility, Needle Driver, Brachytherapy.

## I. INTRODUCTION

Subcutaneous needle, catheter and electrode insertion is one of the most common minimally invasive procedures [1]. Needle placement error can be categorized as intrinsic and extrinsic ones. For intrinsic ones, needle deflection due to tissue-needle interaction causes the deviation of needle tip from the target. Intra- and post-operative edema induces implanted seed drift for procedures like brachytherapy. For extrinsic errors, perturbations are caused by patient movement, respiratory motion, and external surgical tool caused tissue deformation (e.g. ultrasound probe), etc. To compensate these errors is one of the major motivations of deploying active needle steering. The proposed needle driver is capable of steering bevel tip needle and active cannula while with a clinical application on prostate brachytherapy.

Early MRI-guided prostate robots focus on manual actuation. There is active work being developed in the area

H. Su, G.A. Cole and G.S. Fischer are with Automation and Interventional Medicine (AIM) Robotics Laboratory, Department of Mechanical Engineering, Worcester Polytechnic Institute, 100 Institute Road, Worcester, MA 01609, USA [haosu, gfischer]@wpi.edu

M. Zervas and C. Furlong are with Center for Holographic Studies and Laser micro-mechaTronics (CHSLT) and NanoEngineering, Science and Technology (NEST), Department of Mechanical Engineering, Worcester Polytechnic Institute, 100 Institute Road, Worcester, MA 01609, USA

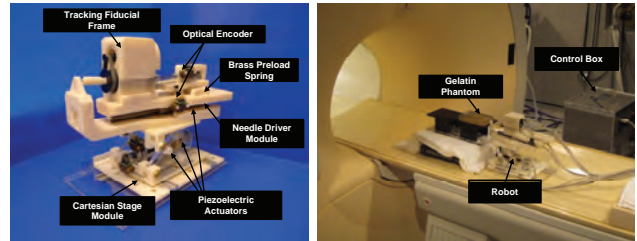


Fig. 1. (Left) Physical prototype of 6-DOF piezoelectric actuated needle placement robot consisting of needle driver module and Cartesian gross positioning module. The needle driver module provides 8cm insertion stroke, 5cm stylet retraction stroke and 40 revolutions per minute rotation speed. The Cartesian gross positioning module provides 8cm axial motion, 3cm elevation and 4cm lateral motion. (Right) The robot prototype in the bore of a 3T MRI scanner with a phantom.

of pneumatically actuated robotic devices [2]. Stoianovici *et al.* described a MRI-compatible pneumatic stepper motor and applied it to robotic brachytherapy seed placement [3]. Our previous work presented a pneumatic servo system and sliding mode control [4], [5]. Kokes *et al.* [6] reported a pneumatic needle driver system for radio frequency ablation of breast tumors. Song *et al.* [7] reported a pneumatically actuated modular robotic system with parallel mechanism.

Pneumatic actuation does have a low level of image interference, however the scalability, simplicity, size and inherent robustness of electromechanical systems present a clear advantage over pneumatically actuated systems. To this end, Chinzei *et al.* [8] developed a general-purpose robotic assistant with ultrasonic motors. Goldenberg *et al.* [9] presented targeting accuracy and MRI compatibility tests for a MRI-guided robot employing ultrasonic actuators for close-bore MRI scanners. Due to unacceptable signal noise from the motor, the motor was disabled during the scanning. Krieger *et al.* [10] recently designed a transrectal prostate robot actuated by piezoelectric motors with 40%–60% SNR reduction under motion.

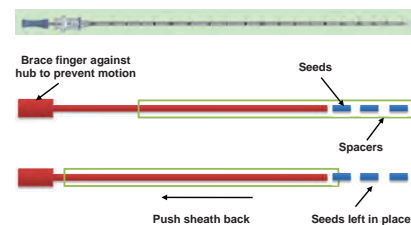


Fig. 2. (Top) Brachytherapy Needle from CP Medical, (bottom) schematic of preloaded needles: after insertion, the sheath is withdrawn over the stylet, leaving the seeds in the place (modified from [11]).

However, no prior work has investigated piezoelectric actuated robotic systems for needle steering under real-time high-field continuous MRI. With its many merits, in a transperineal manner which alleviates the requirement to perform the implant procedures in a different pose than used for preoperative imaging. Our ultimate overall goal is to develop a teleoperated needle placement system consists of a slave needle placement robot and a fiber optic force sensor to achieve prostate intervention under continuous high-field MRI. Hence, the contributions of the paper are (1) the first demonstration of a 6-DOF needle placement robot with steering capability under real-time 3T MRI guidance with less than 2% SNR loss at full speed during imaging, and (2) opto-mechanical design of a high-resolution fiber optic force sensor to measure needle insertion force and render haptic display.

This paper is organized as follows: Section II describes the system requirements and mechanism design including system architecture, robot structure and optical tracking frame. Section III presents the controller electrical design and system setup. Fiber optic sensing principle and opto-mechanical design are presented in Section IV. Phantom experiment in a 3T close MRI bore and sensor calibration are presented in Section V. Section VI concludes the paper with discussion and future work.

## II. NEEDLE DRIVER MECHANISM DESIGN

### A. System Concept and Specifications

Besides the MRI compatibility constraint, there are following design considerations:

1) Motion degree of freedom: 3-DOF motion needle driver and 3-DOF Cartesian gross positioning stage as shown in Fig. 1. A coarse to fine architecture decouples the motion and simplifies the kinematics, while guaranteeing high targeting accuracy. As shown in Fig. 2 top, the clinical 18Gauge needles for prostate brachytherapy have an inner stylet and hollow sheath. Radioactive seeds are pre-loaded with 5.5mm spacers between them before starting the surgery. During the insertion, one hand holds the cannula and the other hand brace against stylet hub to prevent relative motion. After insertion, the sheath is withdrawn over the stylet while leaving the seeds in place. To mimic the physician preload needle type brachytherapy procedure, the needle driver provides 1-DOF cannula rotation about its axis with 1-DOF translational insertion. Another 1-DOF of translational stylet motion is implemented to coordinate the motion with respect to the cannula. The rotation motion of the cannula may be used for bevel-based steering to limit deflection [12] or may be used for active cannula [13].

2) Operation in confined space: when the patient lies in the scanner bore with semilithotomy position, the lateral space between the legs is around 8cm. To fit into this space, the width of the needle driver module has a wedge shape with 6cm front width (10cm long) and 10cm back width (25cm long).

3) Sterilization: only the plastic tip guide, collet, nut and guide sleeve have direct contact with the needle and are

removable and sterilizable.

### B. System Architecture

Three-dimensional surgical navigation software 3D Slicer serves as a user interface with the robot. The navigation software is running on a Linux-based workstation in the scanner's console room. The system workflow follows a preoperative planning, optical frame registration, targeting and verification. OpenIGTLink [14] is used to exchange control, position, and image data. To perform dynamic global registration between the robot and scanner, a passive tracking the fiducial frame is integrated to the robot as shown in Fig. 3.

### C. Universal Needle Clamping and Loading Mechanism

To design a needle driver that allows a large variety of standard needles to be used, a new clamping device rigidly connect the needle shaft to the driving motor mechanism is developed as shown in Fig. 3. It consists of three components made of ABS plastic: collet, collet nut and collet screw shaft. This structure is a collet mechanism and a hollow screw is twisted to fasten the collet thus rigidly locks the needle shaft on the clamping device. The clamping device is connected to the rotary motor through a timing belt. An eccentric pulley tensioner that is concentric with the rotary piezoelectric motor can freely adjust the distance between the motor and the clamping mechanism. The clamping device is generic in the sense that each collet can accommodate a wide range of standard medical needle diameters. The overall needle diameter range for three collets is from 25 Gauge (0.5144mm) to 16 Gauge (1.651mm). By this token, it can not only fasten brachytherapy needles but also biopsy needle or most other standard needles instead of designing some specific structure to hold the needle as those in [15]. The plastic needle guide with quick release mechanism, collet, nut and guide sleeve have direct contact with the needle and are low cost and disposable.

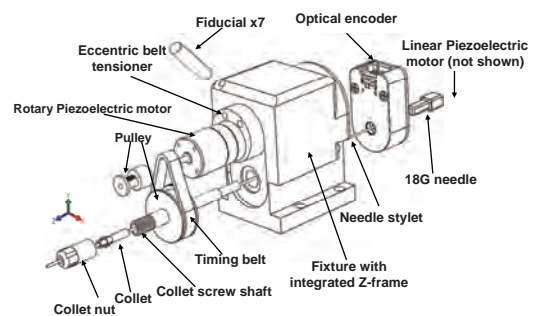


Fig. 3. A exploded view of the needle clamping mechanism, fiducial tracking frame and rotary motor fixture with timing belt tensioner.

Since the linear motor for controlling the inner stylet with respect to the outer cannula is collinear with the collet and shaft (Fig. 3), it is necessary to offset the shaft to manually load the needle. A brass spring preloaded mechanism (Fig. 1) is proposed which provides lateral passive motion freedom. The operator can pinch the mechanism and offset the top

motor fixture then load needle and lock with the needle clamping. This structure allows for easy, reliable and rapid loading of standard needles.

### III. NEEDLE DRIVER ELECTRICAL DESIGN

#### A. Hardware Architecture

The PiezoMotor actuators (Uppsala, Sweden) chosen are non-harmonic piezoelectric motors, which have two advantages over a harmonic drive: the noise caused by the driving wave is much easier to suppress, and the motion produced by the motors is generally at a more desirable speed and torque. Optical encoders (US Digital, Vancouver, Washington) have been thoroughly tested in a 3T MRI scanner with satisfactory performance.

#### B. Piezoelectric Actuator Driver

Custom motor driver boards were developed [16], because commercially available hardware to drive piezoelectric motors do not consider the MRI frequency interference problem, and it is generally not possible to drive the motors with highly specific arbitrary waveforms without interference to the scanner. The driver is a 4 channel high power arbitrary waveform generator designed to run piezoelectric actuators. Waveform tables are loaded over USB or from SD card by a companion co-processor who is responsible for bootstrapping and provisioning the FPGA.

### IV. FABRY-PEROT INTERFERENCE FIBER OPTIC SENSOR

It is reported in [17] that force sensing range for prostate brachytherapy is within 20 Newton and a resolution of 0.01 Newton is sufficient. Due to the loss of tactile feedback in a teleoperated needle placement robot [18], a 1-DOF fiber optic force sensor that measures *in vivo* needle insertion forces is proposed based on our previous effort [19] to render proprioception associated with brachytherapy.

A number of fiber optic force sensors for MRI applications based on light intensity modulation have been proposed [20], [21], to name a few. Due to the limited space in the robot design, there is a need to miniaturize the sensor while retain the sensing range and resolution requirement. Fiber Bragg Grating (FBG) sensors seem to be a viable solution. FBG directly correlate the wavelength of light and the change in the desired strain. If the fiber is strained from applied loads then these gratings will change accordingly and allow a different wavelength to be reflected back from the fiber. However, the costly optical source, FBG fibers and spectral analysis equipment present formidable application for medical instrumentation. Fabry-Perot interference (FPI) fiber optic sensor provides an amiable solution for high-resolution force sensing that only relies on simple interference pattern based voltage measurement.

#### A. Principle of Fabry-Perot based Fiber Optic Sensor

In a Fabry-Perot strain sensor, light propagates through a cavity containing semi-reflective mirrors. Some light is transmitted and some is reflected. As shown in the top of

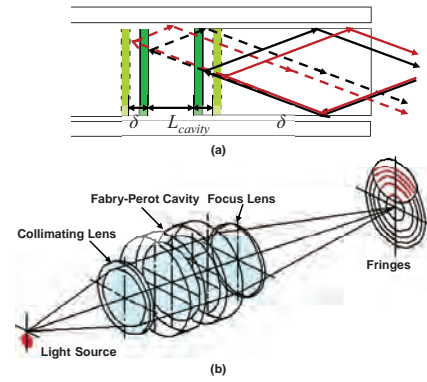


Fig. 4. Fabry-Perot sensing principle. (Top) light propagation in Fabry-Perot cavity, (bottom) resulting fringe pattern.

Fig. 4, the distance between the two fiber tips is generally on the order of nanometers and, depending on the gauge length (the active sensing region, defined as the distance between fusion welds).  $L_{cavity}$  is the original cavity length.  $\delta$  is the change in the cavity length from a given load. The returning light interferes resulting in black and white bands known as fringes (Fig. 4 bottom) caused by destructive and constructive interference. The intensity of these fringes varies due to a change in the optical path length related to a change in cavity length when uni-axial force is applied.

This phenomenon can be quantified through the summation of two waves [22]. By multiplying the complex conjugate and applying Euler's identity, we obtain the following equation of reflected intensity at a given power for planar wave fronts:

$$I = A_1^2 + A_2^2 + 2A_1A_2\cos(\phi_1 - \phi_2) \quad (1)$$

with  $A_1$  and  $A_2$  representing the amplitude coefficients of the reflected signals. The above equation can be changed to represent only intensities by substituting  $A_i^2 = I_i (i = 1, 2)$  and  $\phi_1 - \phi_2 = \Delta\phi$  as

$$I = I_1 + I_2 + 2\sqrt{I_1I_2}\cos\Delta\phi \quad (2)$$

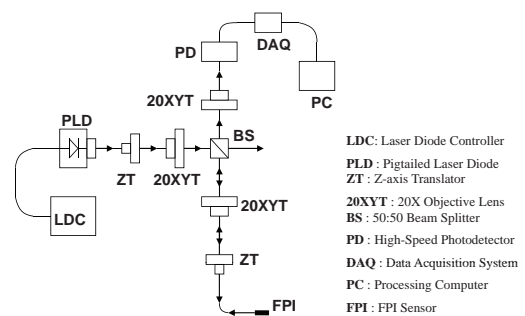


Fig. 5. Schematic diagram of the opto-mechanical design to implement FPI sensor.

An FPI fiber optic strain sensor (FISO Technologies, Canada) was used to evaluate the systems resolution and

potential integration into the robot. The main component of the FPI is the sensing cavity, measuring  $15.8\mu\text{m}$  wide. A glass capillary covering the sensing region is fusion welded to the fiber in two locations and encapsulates the sensor. There is an air gap of approximately  $100.5\mu\text{m}$  wide. The total length of the FPI sensor, including the glass capillary, and bare fiber is approximately  $20\text{mm}$ . Besides immune to electromagnetic and RF signal and substantially cheaper than FBG, the advantages of this sensor includes: 1) static/dynamic response capability, 2) high sensitivity and resolution, 3) no interference due to cable bending and 4) robust to a large range of temperature variation ( $-40^{\circ}\sim 250^{\circ}$ ) due to air gap insulation to the sensing region.

### B. Opto-mechanical Design

As depicted in Fig. 5, the opto-mechanical design of the prototype begins with a pigtailed laser diode (PLD) which emits light in the  $830\text{nm}$  band of the infrared line with a power of  $1\text{mW}$ . This diode is controlled by a laser diode controller (LDC) (ITC-502, ThorLabs Inc, USA) which has a PID built in which helps stabilize the temperature and current of the diode when attached to laser cooler. The output of the pigtailed laser that exits the FC connector (FC) at the end of the sensor's fiber is connected to a  $Z$  axis translator (ZT). This  $Z$  axis translator helps focus the divergent light onto a  $20X$  objective lens (Olympus, Japan) mounted to an  $X - Y$  axis translator (20XYT). This collimated light is sent into a  $50 : 50$  beam splitter cube (BS) (BS017, Thorlabs Inc, USA) where  $50\%$  of the light is split towards the FPI sensor and the other  $50\%$  is not used.

The light that is sent to the sensor is focused onto the  $50\mu\text{m}$  core of the sensor's multi-mode fiber. This focusing is accomplished with the help of another  $20X$  objective lens mounted to an  $X - Y$  axis translator which focuses the light onto the fiber core which is able to adjust via a  $Z$ -axis translator which has the FPI fiber's ST connector (ST) attached to it. The light travels through the fiber and into the sensing cavity and then back reflects out the same optical axis it came in. This back reflected light passes through the  $20X$  objective lens and is collimated into the beam splitter and once through the beam splitter the light is sent into the photodetector (PD) (DET10A, Thorlabs Inc, USA). The photodetector's output is digitized by a 16-bit data acquisition system (DAQ) (USB 6229-BNC, National Instruments, USA) and a processing computer (PC) is used to calculate the strain values.

### C. Force Sensing Design

Due to negligible friction force between the needle and needle guide, the reaction forces between the mechanism (top plate) and the actuator drive rod is used to measure needle insertion force as shown in the top of Fig. 6. The beam to hold the actuator rod has a small  $1.59\text{mm}$  groove to lay the sensor that would extend  $30\text{mm}$  along its side where the FPI sensor could be embedded. The appropriate length was provided to ensure that the PVC fiber covering would be secured to the top plate and provide added durability

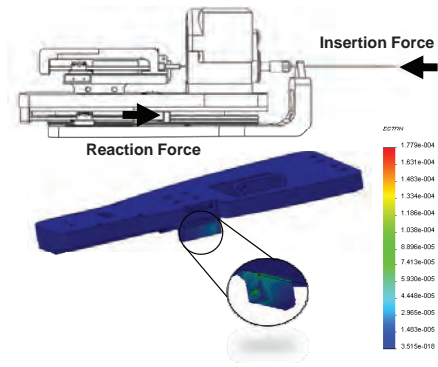


Fig. 6. (Top) needle insertion force measurement based on motor interaction force. (bottom) finite element analysis of ABS top plate under 10 Newton axial force.

to the sensor. Because each friction driven piezoelectric actuator can provides  $12\text{Newton}$  force, the insertion translational motion is provided by two linear motors. In terms of the insertion force range,  $10\text{Newton}$  interaction force is the maximum required for each sensor. The finite element analysis in Fig. 6 illustrates the maximum strain  $100\mu\epsilon$  under  $10\text{ Newton}$  axial force using ABS plastic material with a Young's Modulus of  $2\text{GPa}$  and Poisson's ratio  $0.34$ .

## V. EXPERIMENTS AND RESULTS

To demonstrate the system MRI compatibility of this architecture and the designed piezoelectric driver, a series of MRI phantom tests were performed. The sensing capability of FPI sensor was also demonstrated by experiment.

### A. MRI Compatibility Verification

The MRI compatibility of the needle placement robot was demonstrated in a Philips Achieva 3T system. The phantom employed in the experiment was a  $12\text{cm}$  diameter plastic tube filled with a copper sulfate solution. The motor and encoder were placed immediately adjacent to the left side of the coil. The controller was placed approximately  $3\text{m}$  from the scanner bore.

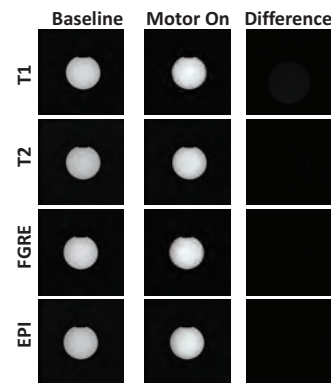


Fig. 7. Representative results showing the difference in images obtained of baseline and motor running conditions. Different with the results in [9] and [10], this demonstrates the real-time *in situ* needle steering capability.

Four imaging protocols were selected for evaluation of compatibility of the system: 1) diagnostic imaging T1-weighted fast gradient echo (T1 FGE/FFE), 2) diagnostic imaging T2-weighted fast spin echo (T2 FSE/TSE), 3) high-speed real-time imaging fast gradient echo (FGRE), and 4) functional imaging spin echo-planar imaging (SE EPI). All sequences were acquired with a slice thickness of  $5mm$  and a number of excitations (NEX) of one. Three configurations were evaluated and used in the comparison: 1) baseline of the phantom only, 2) motor unpowered with controllers DC power supply turned on, 3) motor on and robot is in motion. Eight slices were acquired per imaging protocol for each configuration. Images obtained during motor operation in the scanner are subtracted from the baseline images, as shown in Fig. 7. For statistical analysis, SNR is utilized as the metric for evaluating MRI compatibility with baseline phantom image comparison [23]. Statistical analysis with a Tukey Multiple Comparison confirms that no pair shows significant signal degradation with a 95% confidence interval.

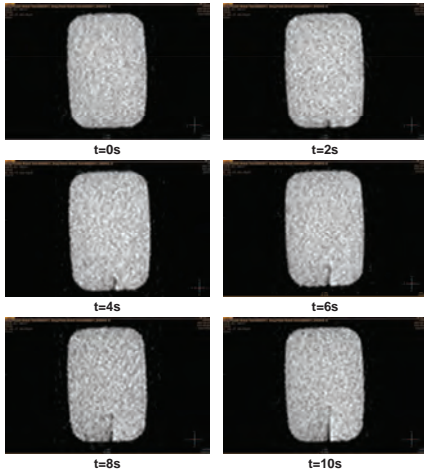


Fig. 8. Bevel tip needle insertion snapshots during 3T echo-planar imaging at 0.4 second interval.

### B. Needle Insertion and Steering under Real-Time MRI-Guidance

A series of experiments are performed to evaluate the system performance for needle insertion and steering capability under real-time 3T MRI-guidance.

The first test is the dynamic needle insertion. Gelatin ( $12cm$  length,  $9cm$  width and  $5cm$  thickness) is utilized as a tissue phantom for in vitro needle steering. The gelatin was mixed with boiling water at a ratio of 1 to 1. A  $22Gauge$  medical needle ( $0.82mm$  outer diameter) with  $45^\circ$  bevel tip is used for steering test. Functional imaging spin echo-planar imaging (field of view  $240mm$ , echo time  $1ms$ , repetition time  $2ms$ , flip angle  $20^\circ$ ) is utilized to monitor the real-time needle motion. This imaging protocol provides approximately  $2Hz$  update rates. Needle insertion motion without needle rotation is controlled by closed-loop optical encoder feedback with proportional-integral-derivative controller. Fig. 8 depicts six bevel tip needle insertion snapshots during 3T

echo-planar imaging at 0.4 second interval. The needle shaft and tip trajectories are clearly visualized in the phantom image without major interference during robot motion.

In the second test, the same  $22Gauge$  medical needle is used to demonstrate the steering capability with MRI visualization. The bevel tip is rotated toward left before insertion. T2-weighted fast spin echo (field of view  $240mm$ , echo time  $90ms$ , repetition time  $3000ms$ , flip angle  $90^\circ$ ) illustrates the final needle shape and tip position. The same procedure is repeated for bevel right before insertion and the results are shown in Fig. 9. There is no visually identifiable interference during needle robot controlled insertion.

All the three tests demonstrate the *in situ* piezoelectric actuation capability in 3T MRI, thus enables real-time needle steering. The compatibility performance and dynamic needle insertion result is significant comparing with the ones in [9] and [10], which have 40% – 60% SNR reduction under motion and must interleave motion with imaging.

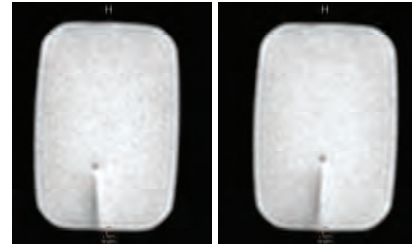


Fig. 9. Bevel tip needle steering image in 3T MRI. (Left) bevel left needle insertion and (right) bevel right needle insertion .

### C. Fiber Optic Force Sensor Calibration

Calibration was performed by attaching the FPI to a manufactured ABS cantilever beam. Strain on the beam was calculated in terms of the applied force  $F$ :

$$\epsilon_{xx} = \frac{12FLc}{bt^3E} \quad (3)$$

where  $L$  is the length of the beam,  $c$  is the distance from the center of the beam along the  $y$ -direction,  $b$  is the width of the base,  $t$  is the thickness, and  $E$  is Young's modulus.

In order to calibrate the FPI, the relationship between the intensity of light at the output and the strain was derived. A hanger system was employed at the end of the cantilever beam to statically apply the load in increments of the 5 grams.

Recall in equation 2, the change in phase  $\Delta\phi$  of the intensity equation is equal to the wave number  $\frac{2\pi}{\lambda}$ , multiplied by the length of the sensing cavity region and the strain in the  $x$ -direction:

$$\Delta\phi = \frac{2\pi(\epsilon_{xx}L_{cavity})}{\lambda} \quad (4)$$

This value for the change in phase was substituted into intensity equation and it is now possible to predict the output intensity of light as a function of the induced strain:

$$I = 2I_0[1 + \cos(\frac{2\pi(\epsilon_{xx}L_{cavity})}{\lambda})] \quad (5)$$

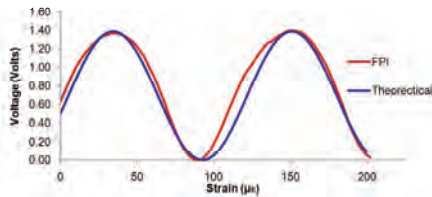


Fig. 10. Calibration results showing voltage versus strain of the FPI sensor together with the theoretical model.

The calibrated system can be seen in the voltage-strain graph shown in Fig. 10. The theoretically predicted relationship is superimposed in the figure. The output voltage follows a sinusoidal pattern that repeats over an increasing applied force. The discrepancy between the measurement and theoretical model is due to the ambient light disturbance to the opto-mechanical prototype which is not shielded during experiment. A gage factor of  $47.48\text{mv}/\mu\epsilon$  was calculated and when using a 16 bit data acquisition system.

## VI. CONCLUSION

This paper presents the design of a MRI compatible piezoelectric actuated 6-DOF robot integrated with a high-resolution fiber optic force sensor for image guided brachytherapy. The MRI compatibility test of the robot and the calibration result of the sensor demonstrate the real-time piezoelectric actuation and sensing capability. The next step of this work will focus on packaging the opto-mechanical system and attain robust and portable interface with the robot controller. Needle steering with the proposed robot prototype will be performed to demonstrate the targeting accuracy in live tissue. Sensor hysteresis, fluctuation and drift would be further investigated with multiple needle insertions and retractions.

## VII. ACKNOWLEDGMENTS

This work is supported in part by the Congressionally Directed Medical Research Programs Prostate Cancer Research Program New Investigator Award W81XWH-09-1-0191. We are grateful for the material support from Igus, Inc.

## REFERENCES

- [1] N. Abolhassani, R. Patel, and M. Moallem, "Needle insertion into soft tissue: A survey," *Medical Engineering and Physics*, vol. 29, no. 4, pp. 413 – 431, 2007.
- [2] G. S. Fischer, A. Krieger, I. I. Iordachita, C. Csoma, L. L. Whitcomb, and G. Fichtinger, "MRI Compatibility of Robot Actuation Techniques – A Comparative Study," *Int Conf Med Image Comput Assist Interv*, Sept. 2008.
- [3] D. Stoianovici, D. Song, D. Petrisor, D. Ursu, D. Mazilu, M. Muntener, M. Mutener, M. Schar, and A. Patriciu, "MRI Stealth robot for prostate interventions.," *Minim Invasive Ther Allied Technol*, vol. 16, no. 4, pp. 241–248, 2007.
- [4] Y. Wang, H. Su, K. Harrington, and G. Fischer, "Sliding mode Control of piezoelectric valve regulated pneumatic actuator for MRI-compatible robotic intervention," in *ASME Dynamic Systems and Control Conference - DSCC 2010*, (Cambridge, MA, USA), 2010.
- [5] H. Su and G. S. Fischer, "High-field MRI-Compatible needle placement robots for prostate interventions: pneumatic and piezoelectric approaches," in *Advances in Robotics and Virtual Reality* (T. Gulrez and A. Hassanien, eds.), Springer-Verlag, 2011.

- [6] R. Kokes, K. Lister, R. Gullapalli, B. Zhang, A. MacMillan, H. Richard, and J. Desai, "Towards a teleoperated needle driver robot with haptic feedback for RFA of breast tumors under continuous MRI," *Medical Image Analysis*, vol. 13, no. 3, pp. 445 – 55, 2009/06/.
- [7] S.-E. Song, N. Cho, G. Fischer, N. Hata, C. Tempany, G. Fichtinger, and I. Iordachita, "Development of a pneumatic robot for MRI-guided transperineal prostate biopsy and brachytherapy: New approaches," in *Robotics and Automation (ICRA), 2010 IEEE International Conference on*, pp. 2580 –2585, May 2010.
- [8] K. Chinzei and K. Miller, "Towards MRI guided surgical manipulator.," *Med Sci Monit*, vol. 7, no. 1, pp. 153–163, 2001.
- [9] A. Goldenberg, J. Trachtenberg, W. Kucharczyk, Y. Yi, M. Haider, L. Ma, R. Weersink, and C. Raoufi, "Robotic system for closed-bore MRI-guided prostatic interventions," *Mechatronics, IEEE/ASME Transactions on*, vol. 13, pp. 374 –379, Jun. 2008.
- [10] A. Krieger, I. Iordachita, S.-E. Song, N. Cho, P. Guion, G. Fichtinger, and L. Whitcomb, "Development and preliminary evaluation of an actuated MRI-compatible robotic device for MRI-guided prostate intervention," pp. 1066 –1073, May 2010.
- [11] K. Wallner, J. Blasko, and M. Dattoli, *Prostate Brachytherapy Made Complicated*. Smart Medicine Press, 2007.
- [12] M. Mahvash and P. Dupont, "Fast needle insertion to minimize tissue deformation and damage," in *Proc. IEEE International Conference on Robotics and Automation ICRA 2009*, pp. 3097 – 3102, 2009.
- [13] D. Rucker and R. Webster, "Mechanics of bending, torsion, and variable precurvature in multi-tube active cannulas," in *Proc. IEEE International Conference on Robotics and Automation ICRA 2009*, pp. 2533 – 7, 2009.
- [14] J. Tokuda and G. Fischer, "OpenIGTLink: an open network protocol for image-guided therapy environment," *Int J Med Robot*, vol. 5, pp. 423–34, Dec. 2009.
- [15] H. S. Bassan, R. V. Patel, and M. Moallem, "A novel manipulator for percutaneous needle insertion: Design and experimentation," *IEEE/ASME Transactions on Mechatronics*, vol. 14, no. 6, pp. 746 – 761, 2009.
- [16] G. Cole, K. Harrington, H. Su, A. Camilo, J. Pilitsis, and G. Fischer, "Closed-Loop Actuated Surgical System Utilizing Real-Time In-Situ MRI Guidance," in *12th International Symposium on Experimental Robotics - ISER 2010*, (New Delhi and Agra, India), Dec 2010.
- [17] Y. Yu, T. Podder, Y. Zhang, W. S. Ng, V. Mistic, J. Sherman, L. Fu, D. Fuller, E. Messing, D. Rubens, J. Strang, and R. Brasacchio, "Robot-assisted prostate brachytherapy," *Medical Image Computing and Computer-Assisted Intervention - MICCAI 2006*, (Berlin, Germany), pp. 41–9, Springer-Verlag, 2006.
- [18] H. Su, W. Shang, G. Cole, K. Harrington, and F. S. Gregory, "Haptic system design for MRI-guided needle based prostate brachytherapy," *IEEE Haptics Symposium 2010*, (Boston, MA, USA), IEEE, 2010.
- [19] H. Su, M. Zervas, C. Furlong, and G. Fischer, "A miniature MRI-compatible fiber-optic force sensor utilizing fabry-perot interferometer," in *SEM Annual Conference and Exposition on Experimental and Applied Mechanics*, (Uncasville, CT, USA), 2011.
- [20] H. Su and G. Fischer, "A 3-axis optical force/torque sensor for prostate needle placement in magnetic resonance imaging environments," *2nd Annual IEEE International Conference on Technologies for Practical Robot Applications*, (Boston, MA, USA), pp. 5–9, IEEE, 2009.
- [21] P. Polygerinos, P. Puangmali, T. Schaeffter, R. Razavi, L. Seneviratne, and K. Althoefer, "Novel miniature MRI-compatible fiber-optic force sensor for cardiac catheterization procedures," in *Robotics and Automation (ICRA), 2010 IEEE International Conference on*, pp. 2598 –2603, May 2010.
- [22] T. K. Gangopadhyay, "Prospects for fibre bragg gratings and fabry-perot interferometers in fibre-optic vibration sensing," *Sensors and Actuators A: Physical*, vol. 113, no. 1, pp. 20 – 38, 2004.
- [23] Y. Wang, G. Cole, H. Su, J. Pilitsis, and G. Fischer, "MRI compatibility evaluation of a piezoelectric actuator system for a neural interventional robot," in *Annual Conference of IEEE Engineering in Medicine and Biology Society*, (Minneapolis, MN), pp. 6072–6075, 2009.

---

# High-field MRI-Compatible Needle Placement Robots for Prostate Interventions: Pneumatic and Piezoelectric Approaches

Hao Su<sup>1</sup>, Gregory A. Cole<sup>1</sup> and Gregory S. Fischer<sup>1</sup>

Automation and Interventional Medicine (AIM) Laboratory, Department of Mechanical Engineering, Worcester Polytechnic Institute, Worcester, MA, 01609, USA Email: [haosu, gfischer]@wpi.edu

**Abstract.** Magnetic resonance imaging (MRI) can be a very effective imaging modality for live guidance during surgical procedures. The rationale of MRI-guided surgery with robot-assistance is to perform surgical interventions utilizing "real-time" image feedback while minimize operation time and increase the surgical outcome. However, challenges arise from electromagnetic compatibility in the high-field (1.5T or greater) MRI environment and mechanical constraints due to the confined close-bore space. This paper presents two MRI-compatible approaches for image-guided transperineal prostate needle placement. Described is the robotic mechanism, actuator and sensor design, controller design and system integration for a pneumatically actuated robotic needle guide and a piezoelectrically actuated needle placement robot. The two degree-of-freedom (DOF) pneumatic robot with manual needle insertion has a signal to noise ratio (SNR) loss limited to 5% with alignment accuracy under servo pneumatic control better than  $0.94mm$  per axis. While the 6-DOF piezoelectrically actuated robot is the first demonstration of a novel multi piezoelectric actuator drive with less than 2% SNR loss for high-field MRI operating at full speed during imaging. The preliminary experiments in phantom studies evaluates system MRI compatibility, workflow, visualization and targeting accuracy.

## 1 Introduction

Prostate cancer is the most common male cancer and the second most common type of cancer in human. The estimated new prostate cancer cases (192,280) in 2009 account for 25% incident cases in men in the United States [19]. Each year approximately 1.5 million core needle biopsies are performed, yielding about 220,000 new prostate cancer cases. Over 40,000 brachytherapy radioactive seed implantation procedures are performed in the United States each year, and the number is steadily growing. Prostate specific antigen blood tests and digital rectal exams are the two major preliminary prostate cancer diagnosis methods. However, prostate biopsy is the conclusive approach to confirm cancer diagnosis. Prostate brachytherapy and cryotherapy are often used for early therapy.

2 Hao Su, Gregory A. Cole and Gregory S. Fischer

Transrectal ultrasound (TRUS) is the current “gold standard” for guiding both biopsy and brachytherapy due to its real-time nature, low cost and ease of use. Fig. 1 shows the traditional template-based TRUS-guided approach to brachytherapy seed placement. However, TRUS-guided biopsy has a detection rate of only 20 – 30% [34]. The drawbacks are largely due to the inherent limitation of ultrasound imaging itself and the mechanical template used in the procedure to guide needles. Ultrasound imaging is inferior to MRI for prostate cancer treatment due to its limited resolution and inability to display implanted radiation seeds. Furthermore, ultrasound probe deforms the prostate and induces seed migration. Since the dosimetry plan is usually performed on the manual segmentation of pre-operative ultrasound images, the seed placement accuracy is deteriorated due to the imaging limitation and probe induced tissue deformation. On the other hand, the template used to guide needles in TRUS is a  $6\text{cm} \times 6\text{cm}$  mechanical grid with  $5\text{mm} \times 5\text{mm}$  space distance which limits the entrance location at the perineum and the positioning resolution of needle insertion. In addition, it forbids needle angulation to adjust needle orientation for better targeting or to avoid pubic arch interference (PAI), thus restricting the eligible patient population.

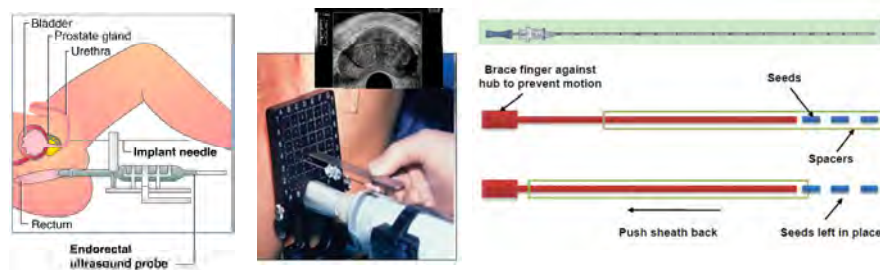


**Fig. 1.** Traditional template-based TRUS-guided approach to prostate brachytherapy (left and middle). Brachytherapy needle from CP Medical and the schematic procedure of preloaded needles: after insertion, the sheath is withdrawn over the stylet, leaving the seeds in the place (modified from [37]) (right).

On the other hand, the MRI-based medical paradigm offers several advantages over other imaging counterparts. First, MRI has a couple of mechanisms to provide high-fidelity soft tissue contrast and spatial resolution. Second, MRI is an essentially three-dimensional imaging modality that permits almost arbitrary imaging plane selection, even in a dynamic manner. Third, MRI produces non-ionizing thus imposes no safety hazard to the patient or practitioner. The clinical efficacy of MRI-guided prostate brachytherapy and biopsy was demonstrated by D’Amico *et al.* at the Brigham and Women’s Hospital using a 0.5T open-MRI scanner [8]. MR images were used to plan and monitor transperineal needle placement. The needles were inserted manually using a guide comprising a grid of holes, with the patient in the lithotomy position, similarly to the TRUS-guided approach.



The motivation of deploying robotic system in prostate interventions comes from three major aspects. First, robot-assisted surgery guarantees good geometric accuracy as it relies upon rigid mechanical structure and motion/force control of the robot, thus overcomes the accuracy limits of traditional mechanical templates ( $5mm$ ) and allows needle angulation. Second, robots can be designed with appropriate scale to fit into open scanner bores or cylindrical closed-bores. Third, since robots are stable and untiring, they can stay inside the scanner bore and perform the interventional procedures with teleoperated control. This eliminates or reduces the necessity of the iterative and time-consuming procedure that usually takes several cycles of imaging for registration inside bore, interventions out of bore (due to space limit) and confirmation inside bore. In general, MRI-guided surgery with robot-assistance can ultimately minimize operation time while increases the surgical outcome, thus greatly reduces the equipment cost and overhead.

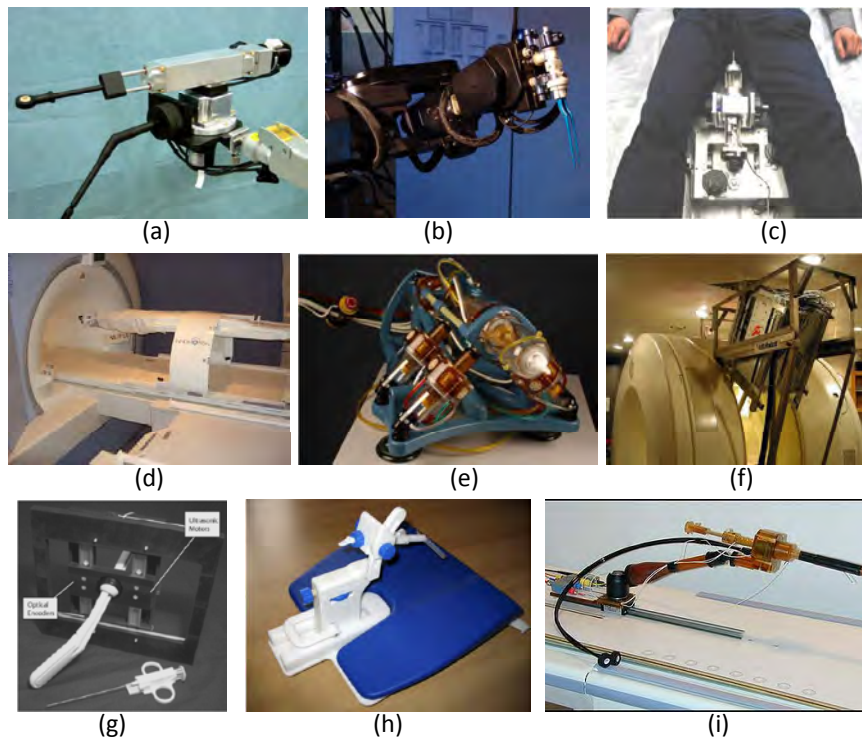


**Fig. 2.** MRI guided robots and assistance device: Masamune *et al.* [22] (a), Sutherland *et al.* [32](b), Goldenberg *et al.* [17] (c), INNOMOTION [23] (d), Stoianovici *et al.* (e), Chinzei *et al.* [7] (f), Elhawary *et al.* [11] (g), Beyersdorff *et al.* [3] (h) and Krieger *et al.* [21] (i).

The challenges, however, arise from electromagnetic compatibility in the high-field (1.5T or greater) MRI environment and mechanical constraints due to the con-

finned closed-bore space. The manifestation of the bidirectional MRI compatibility requires that both the device should not disturb the scanner function and should not create image artifacts and the scanner should not disturb the device functionality. Thus, in the actuation level, conventional DC/AC motors that relies on electromagnetism for conventional robotic actuation is not feasible in MRI. In the material level, conductive materials such as metallic components can induce heating thus special means should be taken to avoid the side-effects of these materials or even avoid using them. Moreover, the confined physical space in closed-bore high-field MRI presents stringent challenges for material selection and mechanical design.

Thorough reviews of MRI-compatible systems to date for image-guided interventions are presented by Tsekos, *et al.* [36] and by Elhawary, *et al.* [10]. Fig. 2 shows a collection of the MRI-compatible assistants developed to date. Robotic assistance has been investigated for guiding instrument placement in MRI, beginning with neurosurgery [22]. A most recent MRI-guided neurosurgical robot [32] was developed by Sutherland *et al.* Goldenberg *et al.* [17] proposed an MRI-compatible robotic system for image-guided prostatic interventions. INNOMOTION [23] is the first commercially available MRI-guided robot that utilizes pneumatic actuation and was recently acquired by Synthes<sup>®</sup>. Stoianovici *et al.* [28] described a MRI-compatible pneumatic stepper motor PneuStep, which has a very low level of image interference. Chinzei *et al.* [7] developed a general-purpose robotic assistant for open MRI that was subsequently adapted for transperineal intraprostatic needle placement [9]. Elhawary *et al.* [11] performed transrectal prostate biopsy. Beyersdorff *et al.* [3] performed targeted transrectal biopsy in a 1.5T MRI unit with a passive articulated needle-guide and have reported 12 cases of biopsy to date. Krieger *et al.* [21] presented a 2-DOF passive, un-encoded, and manually manipulated mechanical linkage to aim a needle guide for transrectal prostate biopsy with MRI guidance. Song *et al.* [26] presented a pneumatic robot for MRI-guided transperineal prostate biopsy and brachytherapy.

Generally, there are four actuation principles for MRI applications, namely remote actuation, hydraulic, pneumatic and ultrasonic/piezoelectric actuators [16]. A substantial armamentarium of actuation methods has been studied in a number of image-guided interventions and rehabilitation scenarios. Early MRI-compatible robotic systems focus on manual driven or ultrasonic motor driven and the latter cannot run during imaging due to significant signal loss. Remote actuation suffers from bulky structure, low bandwidth and lower resolution and is not preferable for robotic applications. Hydraulic and pneumatic actuation are considered as the silver bullet for MRI applications in the sense that these system can completely get rid of electrical and magnetic fields inside the scanner by using dielectric materials, thus providing high signal noise ratio. Hydraulic systems renders very large output force, but usually suffer from cavitation and fluid leakage. Pneumatic actuation is easier to maintain and back-drivable due to the compressibility of air and is more favorable for high bandwidth applications, especially ideal for force control. The disadvantages of pneumatic actuation is also because of compressibility of air and the induced time delay, that makes it difficult to control in millimeter level in which the medical robotics usually aims to control and excel than human. Ultrasonic/piezoelectric actuation does not rely upon magnetism, but since there is still high frequency electrical signal and the piezoelectric elements are often embedded inside ferromagnetic or paramagnetic materials, piezoceramic motors using commercially available motor controllers have been evaluated by [11] which negatively impacted image quality. The difficulty arises from the actuator driving controller that usually induces sig-

nificant image artifact using off-the-shelf control circuits. However, the scalability, simplicity, size and inherent robustness of electromechanical systems present a clear advantage over pneumatically actuated systems.

*Generally, no prior work has considered the exploitation of modular robotic systems for in-situ needle placement in high-field closed-bore MRI, with its many merits, in a transperineal manner which alleviates the requirement to perform the implant procedures in a different pose than used for preoperative imaging.* This paper reviews the design of two approaches that comply with the compatibility while address *in-situ* needle placement with reduced cost and system complexity. By leveraging the pneumatic and piezoelectric actuation approaches, the underlying philosophy of this research effort aims to explore the two distinct methods to demonstrate two design examples that provides semi-automatic and teleoperated needle placement robots for prostate interventions. Even the focus of the design targets prostate cancer, this interventional system is possible to be adopted for other similar percutaneous applications.

This chapter is organized as follows: Section 2 analyzes and articulates the design requirement. Section 3 describes the 2-DOF pneumatic needle placement robot design with manual insertion and Section 4 describes the 6-DOF fully actuated needle placement robot design with piezoelectric actuation. Section 5 presents the system architecture and workflow utilizing these two robots. A number of experiments in 3 Tesla closed-bore scanner and analysis are elaborated in Section 6. Finally, a discussion of the system is presented in Section 7 that summarizes the experimental insight and future work.

## 2 Design Requirement

### 2.1 Surgical Procedure Analysis and Design Implication

Robotic design starts from the surgical procedure analysis which provides the guideline and “optimal” solution of designing clinically practical robots. This includes the analysis of prostatic intervention classification based on interventional approach (transrectal, transperineal and transurinal) and the motion analysis of needle insertion during biopsy, brachytherapy and ablation.

The transperineal approach is preferable for the following reasons [4]. First, transrectal approach samples the peripheral zone (the most common location of the cancer) across its smallest dimension and has higher possibility of missing the cancer than the transperineal approach. Second, transrectal method does not allow accessing some regions of the prostate that are blocked by the urethra. Third, the transrectal technique is not extendible to therapy (brachytherapy or cryotherapy) that requires multiple needle placements because of increased rectal injury that causes higher risk of infection.

As shown in Fig. 1 right, the clinical 18Gauge (1.27mm) needles for prostate brachytherapy have an inner stylet and hollow sheath. Radioactive seeds are preloaded with 5.5mm spacers between them before starting the surgery. During the insertion, one hand holds the cannula and the other hand brace against stylet hub to prevent relative motion. After insertion, the sheath is withdrawn over the stylet while leaving the seeds in place. To mimic the physician preload needle type brachytherapy procedure, the needle driver provides 1-DOF cannula rotation about its axis

with 1-DOF translational insertion. Another 1-DOF of translational stylet motion is implemented to coordinate the motion with respect to the cannula. The rotation motion of the cannula may be used for bevel-based steering to limit deflection or may be used for active cannula [40].

## 2.2 System Requirement

The system's principal function is accurate transperineal needle placement in the prostate for diagnosis and treatment, primarily in the form of biopsy and brachytherapy seed placement, respectively. The patient is positioned in the supine position with the legs spread and raised as shown in Fig. 3 (left). The patient is in a similar configuration to that of TRUS-guided brachytherapy, but the typical MRI bore's constraint ( $\leq 60\text{cm}$  diameter) necessitates reducing the spread of the legs and lowering the knees into a semi-lithotomy position. The robot operates in the confined space between the patient's legs without interference with the patient, MRI scanner components, anesthesia equipment, and auxiliary equipment present as shown in the cross-section shown in Fig. 3 (right).

The average size of the prostate is 50mm in the lateral direction by 35mm in the anterior-posterior direction by 40mm in length. The average prostate volume is about 35cc; by the end of a procedure, this volume enlarges by as much as 25% due to swelling [37]. For our system, the standard 60mm  $\times$  60mm perineal window of TRUS-guided brachytherapy was increased to 100mm  $\times$  100mm, in order to accommodate patient variability and lateral asymmetries in patient setup. In depth, the workspace extends to 150mm superior of the perineal surface. Direct access to all clinically relevant locations in the prostate is not always possible with a needle inserted purely along apex-base direction due to PAI. Needle angulation in the sagittal and coronal planes will enable procedure to be performed on many of these patients where brachytherapy is typically contraindicated due to PAI as described by Fu, *et al.* [14].

The robot is situated upon a manual linear slide that positions the robot in the access tunnel and allows fast removal for reloading brachytherapy needles or collecting harvested biopsy tissue. The primary actuated motions of the robot include two prismatic motions which replicate the DOF of a traditional template-base approach, and two rotational motions for aligning the needle axis to help avoid PAI and critical structures. In addition to these base motions, application-specific motions are also required; these include needle insertion, canula retraction or biopsy gun actuation, and needle rotation. The accuracy of the individual servo-controlled joints is targeted to be 0.1mm, and the needle placement accuracy of the robotic system itself is targeted to be better than 1.0mm. This target accuracy approximates the voxel size of the MR images used which represents the finest possible targeting precision. The overall system accuracy, however, is expected to be somewhat less when effects such as imaging resolution, needle deflection, and tissue deformation are taken into account. The MR image resolution is typically 1mm and the clinically significant target is typically 5mm in size (the precision of a traditional TRUS template).

## 2.3 MRI Compatibility Requirements

Significant complexity is introduced when designing a system operating inside the bore of high-field 1.5-3T MRI scanners since traditional mechatronics materials,

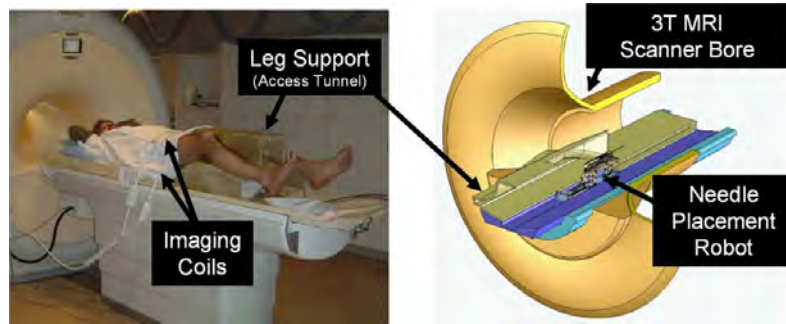


Fig. 2. Positioning of the patient in the simulator. (left) Photograph of the patient lying on a table with a leg support (access tunnel) and imaging coils. (right) 3D schematic diagram of the 3T MRI scanner bore showing the needle placement robot positioned within the leg rest.

a similar configuration to that of TRUS-guided brachytherapy, but the MRI bore's constraint (60 cm diameter) necessitates reducing the spread of the legs and lowering the knees into a semilitotomy position. The robot operates in the confined space between the patient's legs without interference with the patient.

**MR-Safe:** The device, when used in the MR environment, has been demonstrated to present no additional risk to the patient or other individual, but may affect the quality of the diagnostic information. The MR conditions in which the device was tested should be specified in the user manual. The MR conditions in which the device is safe under a set of conditions may not be found to be more extreme MR conditions.

**MR-Compatible:** A device is considered MR-compatible if it is MR safe and if it, when used in the MR environment, has been demonstrated to reduce significantly affected by 35 mm in the anterior-posterior direction by 40 mm in length. The MR conditions in which the device was tested should be specified in conjunction with the term MR-compatible since a device that is safe under one set of conditions may not be found to be so under more extreme MR conditions.

to swelling [26]. For our system, the standard 60 mm  $\times$  60 mm perineal window of TRUS-guided brachytherapy was increased to 100 mm  $\times$  100 mm, in order to accommodate patient variability and lateral asymmetries in patient setup. In depth, the workspace extends to 50 mm superior of the perineal surface.

**Needle Placement Robot: Pneumatic Approach**  
Direct access to all clinically relevant locations in the prostate is not always possible with a needle inserted purely along an apex-base direction due to pubic arch interference (PAI). If more than 25% of the prostate diameter is blocked (typically in prostates larger than 35 cm<sup>3</sup>), then the patient is usually declined for implantation [26]. Needle angulation in the sagittal and coronal planes will enable procedure to avoid a significant majority of these patients who are typically contraindicated for brachytherapy due to PAI.

### B. System Requirements

The kinematic requirements for the robot are derived from the workspace analysis. A kinematic diagram of the proposed system is shown in Fig. 2. The robot is situated upon a manual linear slide that repeatedly positions the robot in the access tunnel and allows fast removal for reloading brachytherapy needles or collecting harvested biopsy tissue. The primary actuated motions of the robot include two prismatic motions and two rotational

device and a safety lock. The latter requires an additional controlled linear motion to accommodate the cannula retraction to release the brachytherapy seeds. Rotation of the needle about its axis may be implemented to either “drill” the needle in to limit deflect, or to steer the needle using bevel steering techniques such as those described in [40]. Sterility has been taken into consideration for the design of the end effectors. In particular, the portions of the manipulator and leg rest that come in direct contact with the patient or needle will be removable and made of materials that are suitable for sterilization. The remainder of the robot will be draped. An alternative solution is to enclose the entire leg rest with the robot in a sterile drape, thus completely isolating the robot from the patient except for the needle.

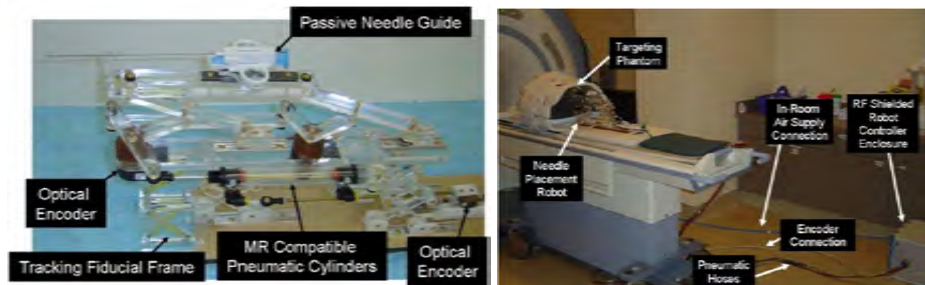


**Fig. 4.** Pneumatic robotic needle placement mechanism with two active DOF and one passive, encoded needle insertion. Dynamic global registration is achieved with the attached tracking fiducial (left). The configuration of the robot with the controller in the scanner room (right).

### 3.1 Mechanical Design

The design of the mechanism is particularly important since there are very confined spaces and the robot is constructed without the use of metallic links. The design was developed such that the kinematics can be simplified, control can be made less complex, motions may be decoupled, actuators can be aligned appropriately, and system rigidity can be increased. Based upon analysis of the workspace and the application, the following additional design requirements have been adopted: 1) prismatic base motions should be able to be decoupled from angulation since the majority of procedures will not require the two rotational DOFs; 2) actuator motion should be in the axial direction (aligned with the scanner’s axis) to maintain a compact profile; and 3) extension in both the vertical and horizontal planes should be telescopic to minimize the working envelope.

The primary base DOFs are broken into two decoupled planar motions. Motion in the vertical plane includes 100 mm of vertical travel, and optionally up to  $15^\circ$  of elevation angle. This is achieved using a modified version of a scissor lift mechanism that is traditionally used for plane parallel motion. By coupling two such mechanisms, as shown in Fig. 5 (left), 2-DOF motion can be achieved. Stability is increased by using a pair of such mechanisms in the rear. For purely prismatic, both slides

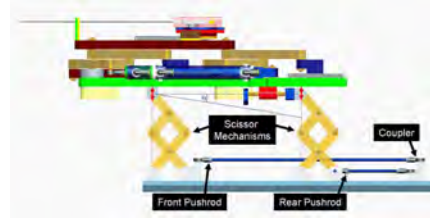


Fig. 3. This mechanism provides for motion in the vertical plane. Coupling the forward and rear motion provides for vertical travel, independently moving the needle.

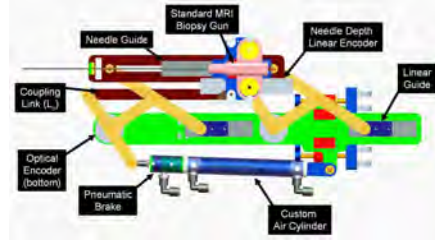


Fig. 4. This mechanism provides for motion in the horizontal plane. The design shown provides prismatic motion only; rotation can be enabled by actuating the actuator. The modular, encoded needle guide senses the depth during manual needle insertion.

forward and rear motion provides for vertical travel, independently moving the needle. The design shown provides prismatic motion only; rotation can be enabled by actuating the actuator. The modular, encoded needle guide senses the depth during manual needle insertion.

rotation can be enabled by actuating the actuator. The modular, encoded needle guide senses the depth during manual needle insertion. The design shown provides prismatic motion only; rotation can be enabled by actuating the actuator. The modular, encoded needle guide senses the depth during manual needle insertion.

rotation can be enabled by actuating the actuator. The modular, encoded needle guide senses the depth during manual needle insertion. The design shown provides prismatic motion only; rotation can be enabled by actuating the actuator. The modular, encoded needle guide senses the depth during manual needle insertion.

rotation can be enabled by actuating the actuator. The modular, encoded needle guide senses the depth during manual needle insertion. The design shown provides prismatic motion only; rotation can be enabled by actuating the actuator. The modular, encoded needle guide senses the depth during manual needle insertion.

rotation can be enabled by actuating the actuator. The modular, encoded needle guide senses the depth during manual needle insertion. The design shown provides prismatic motion only; rotation can be enabled by actuating the actuator. The modular, encoded needle guide senses the depth during manual needle insertion.

rotation can be enabled by actuating the actuator. The modular, encoded needle guide senses the depth during manual needle insertion. The design shown provides prismatic motion only; rotation can be enabled by actuating the actuator. The modular, encoded needle guide senses the depth during manual needle insertion.

rotation can be enabled by actuating the actuator. The modular, encoded needle guide senses the depth during manual needle insertion. The design shown provides prismatic motion only; rotation can be enabled by actuating the actuator. The modular, encoded needle guide senses the depth during manual needle insertion.

C. Actuator Design

3.2 Pneumatic Actuator Design

The MRI environment places severe restrictions on the choice of actuators. Many mechatronic systems use electrodynamic actuation, however, the very nature of an electric motor precludes its use in high-field magnetic environments. Therefore, it is necessary to either use actuators that are compatible with the MR environment, or to use a transmission to mechanically couple the manipulator in close proximity to the scanner to standard actuators situated outside the high field. MR-compatible actuators such as piezoceramic motors have been evaluated in [11, 33];

rotation can be enabled by actuating the actuator. The modular, encoded needle guide senses the depth during manual needle insertion. The design shown provides prismatic motion only; rotation can be enabled by actuating the actuator. The modular, encoded needle guide senses the depth during manual needle insertion.

<sup>1</sup>Airpel E9 Anti-stiction Air Cylinder—<http://www.airpel.com>

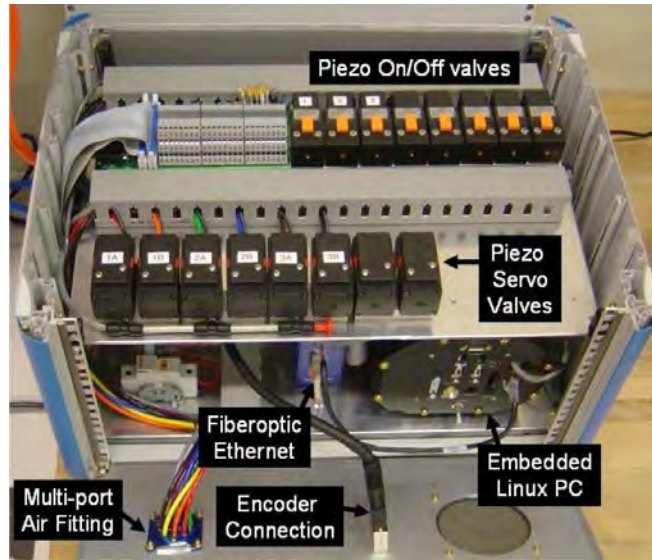


**Fig. 5.** Controller contains the embedded Linux PC providing low-level servo control, the piezoelectric valves, and the fiber-optic Ethernet converter. The EMI shielded enclosure is placed inside the scanner room near the foot of the bed. Connections to the robot include the multi-tube air hose and the encoder cable; connection to the planning workstation is via fiber-optic Ethernet.

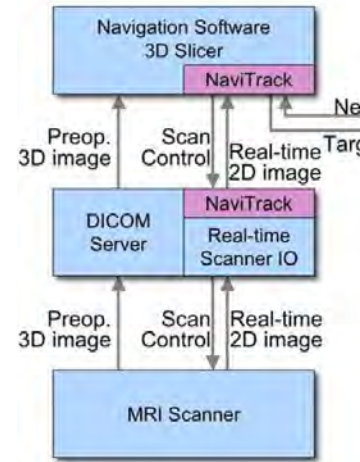


**Fig. 7.** Diagram shows the connection components. NaviTrack, an open-source device exchange control, position, and image data

however, these are prone to introducing noise into MR imaging, and therefore, negatively impacting image quality. Mechanical coupling can take the form of flexible drive shafts [21], push-rod, or hydraulic (or pneumatic) couplings [15].

Pneumatic cylinders are the actuators of choice for this robot. Accurate servo control of pneumatic actuators using sliding mode control has been demonstrated in [5]. Although pneumatic actuation seems ideal, standard pneumatic cylinders are not suitable for use in MRI. Custom MR compatible pneumatic cylinders have been developed for use with this robot. The cylinders are based upon Airpel 9.3 mm cylinders. These cylinders were chosen because the cylinder bore is made of glass and the piston and seals are made of graphite. This design has two main benefits: the primary components are suitable for MRI and they inherently have very low friction (as low as 0.01-N). In collaboration with the manufacturer, we developed the cylinders shown in Fig. 6 (right) bottom that are entirely non-metallic except for the brass shaft. The cylinders can handle up to 100 psi (6.9 bar), and therefore, can apply forces up to 46.8 N. Our newly developed SMC controller has shown submillimeter tracking accuracy using this pneumatic actuator [39].

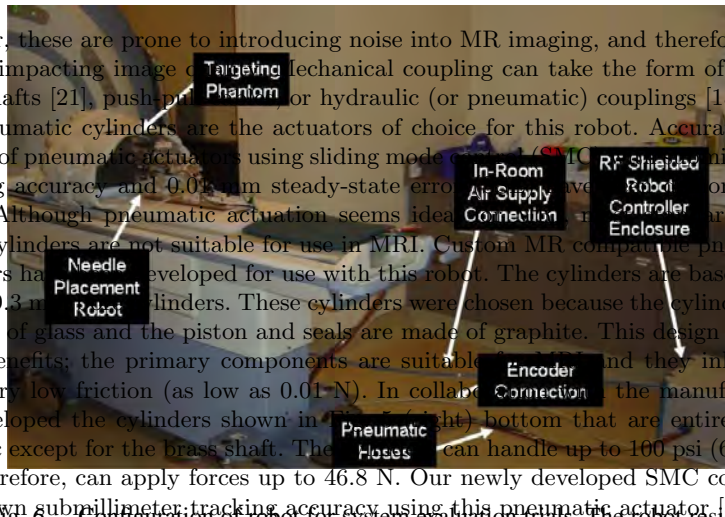
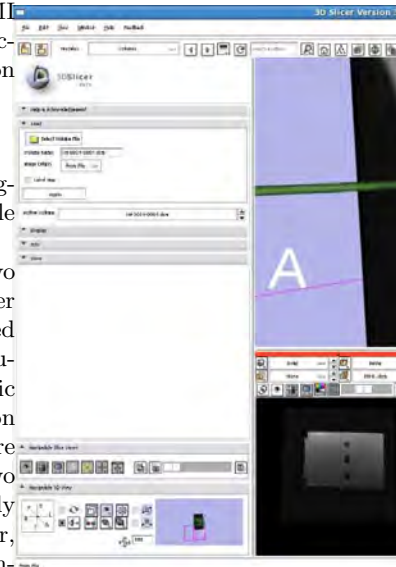


**Fig. 6.** Configuration of robot for system evaluation trials. The robot resides on the table at a realistic relative position to the phantom. The controller operates in a shielded enclosure. In addition to moving the robot, it is important to be able to lock it in position to provide a stable and consistent point from the scanner MR table without the external brakes or significant image quality degradation. The brakes are compact units that attach to the ends of the previously described cylinders, as shown in Fig. 5 (right)



designed for the prostate intervention with the robot is described in [31]. The interface allows smooth operation of the system throughout the clinical workflow including registration, planning, targeting, monitoring, and verification (see Fig. 8). The workstation is connected to the robot and the scanner's console via Ethernet. An open-source device connection and communication tool originally developed in virtual reality research [32] was used to exchange various types of data such as control commands, positional data, and images among the components. Fig. 7 shows the configuration used in the system.

**Fig. 8.** 3-D slicer planning workstation. The real-time readout of the robot's needle position is shown along the needle axis and the sphere represents the patient and the robot are planned. The real-time image of the fiducial frame is acquired from the scanner. The navigation software to calculate the 6-DOF registration, as well as the position and orientation of the robot, is communicated from the navigation software. After the registration, the robot's position is represented in the image (patient's image). During the procedure, a target is defined on the navigation software, and the software translates and aligns the needle guide system, the needle is inserted m



top, and clamp down on the rod. The design is such that the fail-safe state is locked and applied air pressure releases a spring-loaded collet to enable motion. The brakes are disabled when the axis is being aligned and applied when the needle is to be inserted or an emergency situation arises.

Proportional pressure regulators were the valves of choice for this robot because they allow for direct control of air pressure, thus the force applied by the pneumatic cylinder. This is an advantage because it aids in controller design and also has the inherent safety of being able to limit applied pressure to a prescribed amount. Most pneumatic valves are operated by a solenoid coil; unfortunately, as with electric motors, the very nature of a solenoid coil is a contraindication for its use in an MR environment. With pneumatic control, it is essential to limit the distance from the valve to the cylinder on the robot; thus, it is important to use valves that are safe and effective in the MR environment. By placing the controller in the scanner room near the foot of the bed, air tubing lengths are reduced to 5 m. The robot controller uses piezoelectrically actuated proportional pressure valves, thus permitting their use near MRI. A pair of these valves provide a differential pressure of  $\pm 100$  psi on the cylinder piston for each actuated axis. A further benefit of piezoelectrically actuated valves is the rapid response time (4 ms). Thus, by using piezoelectric valves, the robot's bandwidth can be increased significantly by limiting tubing lengths and increasing controller update rate.

### 3.3 Robot Controller Hardware

MRI is very sensitive to electrical signals passing in and out of the scanner room. Electrical signals passing through the patch panel or wave guide can act as antennas, bringing stray RF noise into the scanner room. For that reason, and to minimize the distance between the valves and the robot, the robot controller is placed inside of the scanner room with no external electrical connections. The controller comprises an electromagnetic interference (EMI) shielded enclosure that sits at the foot of the scanner bed, as shown in Fig. 4 right; the controller has proved to be able to operate 3m from the edge of the scanner bore. Inside of the enclosure is an embedded computer with analog I/O for interfacing with valves and pressure sensors and a field programmable gate array (FPGA) module for interfacing with joint encoders (see Fig. 6). Also, in the enclosure are the piezoelectric servo valves, piezoelectric brake valves, and pressure sensors. The distance between the servo valves and the robot is minimized to less than 5 m, thus maximizing the bandwidth of the pneumatic actuators. Control software on the embedded PC provides for low-level joint control and an interface to interactive scripting and higher level trajectory planning. Communication between the low-level control PC and the planning and control workstation sitting in the MR console room is through a 100-FX fiber-optic Ethernet connection. In the prototype system, power is supplied to the controller from a filtered dc power supply that passes through the patch panel; a commercially available MR-compatible power supply will be used in future design iterations. No other electrical connections pass out of the scanner room, thus significantly limiting the MR imaging interference.

12 Hao Su, Gregory A. Cole and Gregory S. Fischer

## 4 Needle Placement Robot: Piezoelectric Approach

The newly developed piezoelectric robot [31], shown in Fig. 7, offers the capability of real-time *in-situ* needle steering in high-field MRI. It consists of a modular 3-DOF needle driver with optical tracking frame coupled similar to that of the pneumatic robot. The modular needle driver simultaneously provides needle cannula rotation and independent cannula and stylet prismatic motion. For experimental purposes, it is shown with a generic MRI-compatible 3-DOF  $x-y-z$  stage; however, application s  
t  
c  
k  
is

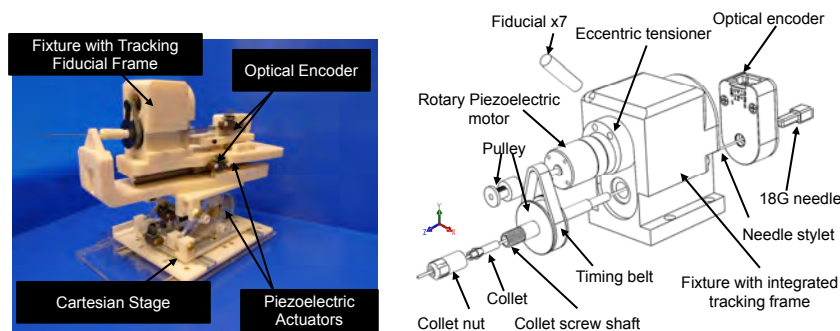


**Fig. 7.** Piezoelectric robotic needle placement mechanism with three DOF needle rotation and collinear translation for prostate brachytherapy on a three DOF Cartesian stage(left). Detailed design of the needle driver platform (right).

The needle placement robot consists of a needle driver module (3-DOF) and Cartesian positioning module (3-DOF). The material is rapid prototyped with ABS and laser cut acrylic. Considering the supine configuration and the robot workspace, the width of the robot is limited to 6cm. As shown in Fig. 7 (left), the lower layer of the needle driver module is driven with linear piezoelectric motor and the upper layer provides cannula rotation motion and stylet prismatic motion.

### 4.1 Mechanical Design

To design a needle driver that allows a large variety of standard needles, a new clamping device shown in Fig. 7 (right) rigidly connects the needle shaft to the driving motor mechanism. This structure is a collet mechanism and a hollow screw made of stereolithography ABS is twisted to fasten the collet thus rigidly locks the needle shaft on the clamping device. The clamping device is connected to the rotary motor through a timing belt that can be fastened by an eccentric belt tensioner. The clamping device is generic in the sense that we have designed 3 sets of collets

and each collet can accommodate a width range of needle diameters. The overall needle diameter range is from 25 Gauge to 7 Gauge. By this token, it can not only fasten brachytherapy needle, but also biopsy needles and most other standard needles instead of designing some specific structure to hold the needle handle.

Once a preloaded needle or biopsy gun is inserted, the collet can rigidly clamp the cannula shaft. Since the linear motor is collinear with the collet and shaft, we need to offset the shaft to manually load the needle. We designed a brass spring preloaded mechanism that provides lateral passive motion freedom. The operator can squeeze the mechanism and offset the top motor fixture then insert the loaded needle through plain bearing housing and finally lock with the needle clamping. This structure allows for easy, reliable and rapid loading and unloading of standard needles.

## 4.2 Piezoelectric Actuator Driver

The piezoelectric actuators (PiezoMotor, Uppsala, Sweden) chosen are non-harmonic piezoelectric motor which have two advantages over a harmonic drive: the noise caused by the driving wave is much easier to suppress, and the motion produced by the motors is generally at a more desirable speed and torque. Even though piezoelectric motor does not generate magnetic field, commercial motor driver boards usually induce significant image artifact due to electrical noise according to the most recent result [20]. A new low noise driver was developed and its architecture is shown in Fig. 8(left) and Fig. 8 (right) shows the configuration of the robot with the controller in the scanner room.

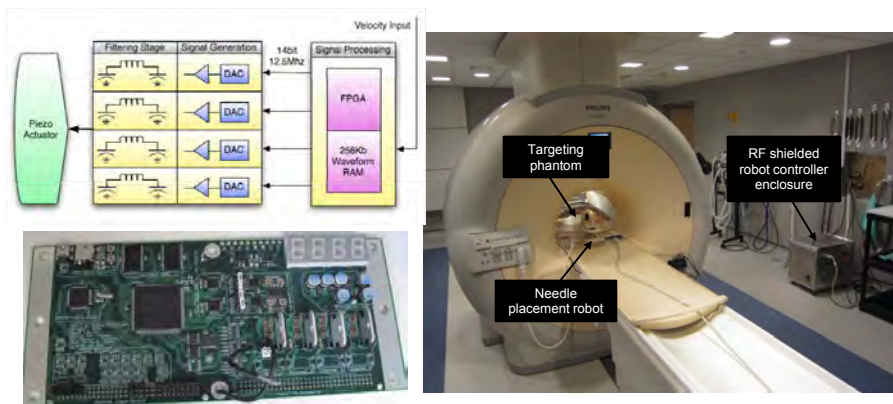


**Fig. 8.** Piezoelectric actuator driver architecture and prototype using FPGA generated waveform (left), and the configuration of the robot with the controller in the scanner room(right).

## 5 Surgical Visualization and Workflow

### 5.1 Surgical Visualization

The user interface for the robot is based on 3D Slicer open-source surgical navigation software (3D Slicer Software, <http://www.slicer.org>). The navigation software runs on a Linux-based workstation in the scanner's console room, and communicates to the robot controller over a fiberoptic connection. A customized graphical user interface (GUI) specially designed for the prostate intervention with the robot is described in [24]. The interface allows smooth operation of the system throughout the clinical workflow including registration, planning, targeting, monitoring and verification (Fig. 9). The workstation is connected to the robot and the scanner's console via Ethernet. OpenIGT Link, open-source device connection and communication tools originally developed for virtual reality research [27], are used to exchange various types of data including control commands, position data, and images among the components. Fig. 10 shows the configuration used in the system as described in [35].

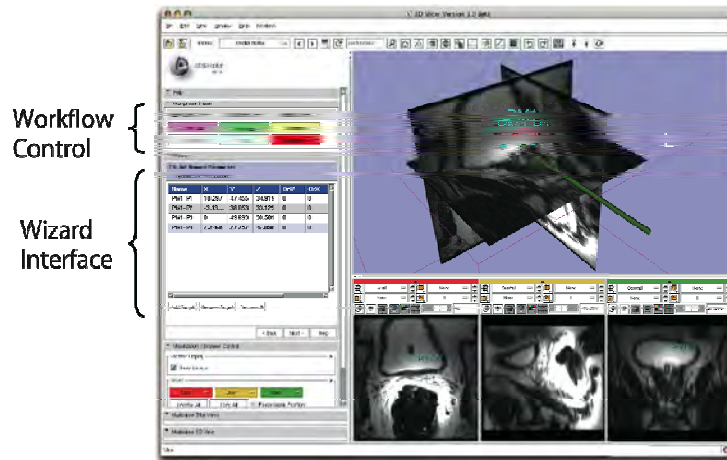


**Figure 3.43** 3D Slicer prostate needle planning interface. The target points are selected, coordinates are transferred to the robot, and the robot moves as the virtual needle glides up and updates in real time

registration algorithms. Evaluation experiments were performed in a 3T GE MRI scanner at BWH. In the planning phase, preoperative images are retrieved from a DICOM server and loaded into the navigation software. Registration is performed between the preoperative planning images and intra-operative imaging using techniques such as those described by Haker, *et al.* [18]. Target points for the needle insertion are selected according to the pre-operative imaging, and the coordinates of the determined target points are selected in the planning GUI. Once the patient and the robot are placed in the MRI scanner, a 2D image of the fiducial frame is acquired and passed to the navigation software to calculate the 6-DOF pose of the robot base using the Z-frame fiducial as described in Section 3.6.2.2. Planning images were acquired for the robot-image registration. The position and orientation of the robot base is

of the phantom and targets selected as shown in Fig. 3.41. Target location and Z-frame fiducial location were sent to the robot in the scanner's RAS coordinates (i.e patient coordinate system). The robot then calculated the required joint positions. When commanded to do so, the robot aligned the needle with real-time feedback of the needle position overlaid on the planning software as shown in Fig. 3.42 (left). The needle is inserted along the

sent through the network from the navigation software to the robot controller. After the registration phase, the robot can accept target coordinates represented in the image (patient) coordinate system in standard Right-Anterior-Superior (RAS) coordinates.

During the procedure, a target and an entry point are chosen on the navigation software, and the robot is sent the coordinates and aligns the needle guide appropriately. In the current system, the needle is inserted manually while the needle position is monitored by an encoded needle guide and displayed in real-time on the display. Needle advancement in the tissue is visualized on the navigation software in two compl

3D image  
images acc  
tinuously  
a high ref  
latter pro  
slower rat

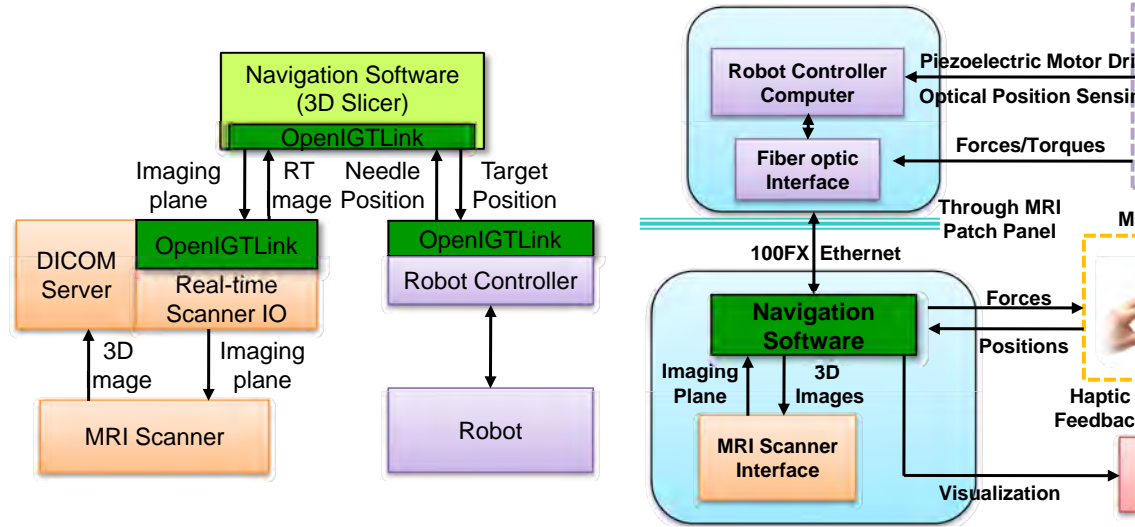


**Fig. 10.** Diagram shows the connection and the data flow among the robot components. OpenIGTLink, an open-source device communication tool, is used to exchange control, position, and image data.

The interface software enables “closed-loop” needle guidance, where the action made by the robot is captured by the MR imaging, and immediately fed back to a physician to aid their decision for the next action. The reason for keeping a human in the loop is to increase the safety of the needle insertion, and to allow for the live MR images to monitor progress. The robot fully aligns the needle as planned before coming in contact with the patient. If necessary, the placement is adjusted

16 Hao Su, Gregory A. Cole and Gregory S. Fischer

responsive to the MR images. The physician performs the insertion under real-time imaging. Fig. 9 shows the planning software with an MR image of the phantom loaded and real-time feedback of the robot position is used to generate the overlaid needle axis model.

## 5.2 Needle Placement Robot Tracking and Localization

Dynamic global registration between the robot and scanner is achieved by passive tracking the fiducial frame in front of the robot as shown in Fig. 7 (right). The rigid structure of the fiducial frame is made of ABS and seven MR Spot fiducials (Beekley, Bristol, CT) are embedded in the frame to form a Z shape passive fiducial. Any arbitrary MR image slicing through all of the rods provides the full 6-DOF pose of the frame, and thus the robot, with respect to the scanner. Thus, by locating the fiducial attached to the robot, the transformation between patient coordinates (where planning is performed) and the needle placement robot is known. To enhance the system reliability and robust, multiple slices of fiducial images are used to register robot position using principal component analysis method. The end effector location is then calculated from the kinematics based on the encoder positions.

## 5.3 System Workflow

The workflow for the system mimics that of traditional TRUS-guided prostate needle insertions, and are as follows:

1. Acquire pre-procedural MRI volume of the patient's prostate and surrounding anatomy.
2. Select specific needle tip targets as shown in Fig. 9.
3. Define corresponding needle trajectories.
4. Acquire an MR image of the robot's tracking fiducial.
5. Register the robotic system to patient/scanner coordinates.
6. Load the biopsy needle or pre-loaded brachytherapy needle into the robot's needle driver.
7. Send coordinates in patient coordinates to the robot.
8. Automatically align the needle guide and lock in place.
9. Manually insert the needle along prescribed axis as virtual needle guide is displayed on real-time MR images intersecting the needle axis.
10. Confirm correct placement.
11. Harvest tissue or deliver therapy.
12. Retract the needle guide and remove biopsy or brachytherapy needle from robot.
13. Update surgical plan as necessary based on volumetric imaging of the prostate and knowledge of the intervention performed.
14. Repeat for as many needles as necessary.

## 5.4 Teleoperated Needle Insertion

Manual insertion was the preferred technique due to the need for tactile feedback during the insertion phase. However, it was found that the ergonomics of manual insertion along this guide proved very difficult in the confines of the scanner bore. The

limited space in closed-bore high-field MRI scanners requires a physical separation between the surgeon and the imaged region of the patient. To overcome the loss of needle tip proprioception information, we are developing a teleoperated haptic system with optical force-torque sensor, to be integrated with a 3-DOF robotic needle driver for MR-guided prostate needle placement. The piezoelectrically actuated robot incorporates tactile feedback and teleoperation. As shown in Fig. 11, an MRI compatible robot controller sits inside the scanner room and communicates to the navigation software and scanner interface running on a laptop in the console room through a fiber optic connection. The optical force sensor interface is incorporated into the in-room robot controller and the needle interaction forces are transmitted back to the navigation software console along with the robot position. We integrate the haptic feedback device into the navigation software framework to provide forces to the operator and control back to the robot.

A direct force feedback architecture [6] would be used to control the teleoperated needle placement system. In this iteration of the system, we employ a commercially available Novint Falcon (Novint Technologies, Inc., Albuquerque, NM) haptic device as the master robot. It has 3 position DOF and can be used to position the needle in the Cartesian space. In the future version, the haptic device would be designed with piezoelectric actuation and optical encoding as shown in Fig. 11. It would be operated inside the scanner room for better observation of patient's physiological condition and other surgical procedures. The human operator positions obtained from the haptic interface are used for trajectory generation and control of the motion of the slave manipulator. The slave robot in this design is the second generation of the 2-DOF pneumatically actuated robotic assistant system which overcomes many design difficulties and promises safe and reliable intraprostatic needle placement inside closed high-field MRI scanners. However, the addition of force feedback allows incorporation of an actuated needle driver and firing mechanism and needle rotation. The contact forces between needle and the tissue are measured by the force/torque sensor [30] and further fed back to the haptic device through its interface.

## 6 Experiments

The first iteration of the needle placement robots has been constructed and is operational. All mechanical, electrical, communications, and software issues have been evaluated. The current state of the pneumatic manipulator is two actuated DOFs (vertical and horizontal) with an encoded passive needle insertion stage. Evaluation of the robot is in three distinct phases: 1) evaluation of the MR compatibility of the robot; and 2) evaluation of the workspace and accuracy. The piezoelectric actuated robot is 6-DOF and the MRI compatibility has been evaluated using similar protocols. This section reports the experimental setup and results of the two robots.

### 6.1 Imaging Protocols

Four imaging protocols as shown in Table 1, were selected for evaluation of compatibility of the system: 1) diagnostic imaging T1-weighted fast gradient echo (T1 FGE/FFE), 2) diagnostic imaging T2-weighted fast spin echo (T2 FSE/TSE), 3)

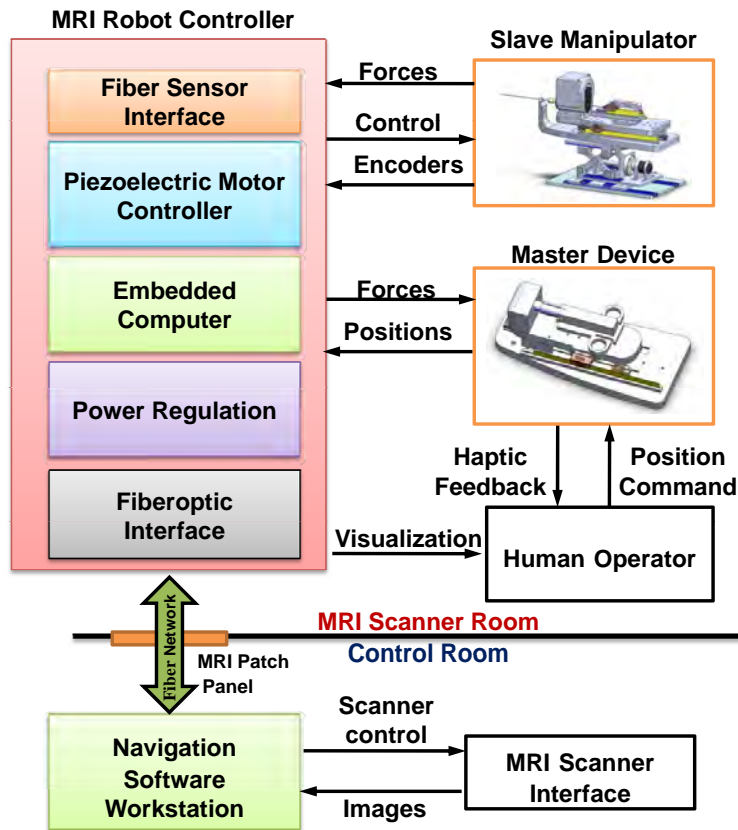


**Fig. 11.** System architecture for the master - slave haptic interface of the piezoelectric robot. The fiber optic force sensor and robot are placed near the isocenter of the MRI scanner, the master manipulator is connected to the navigation software interface, and the two are couple through the robot controller in the scanner room using a fiber optic network connection.

high-speed real-time imaging fast gradient echo (FGRE), and 4) functional imaging spin echo-planar imaging (SE EPI). Details of the scan protocols are shown in Table 1. All sequences were acquired with a slice thickness of 5mm and a number of excitations (NEX) of one. Three configurations were evaluated and used in the comparison: 1) baseline of the phantom only, 2) motor powered with controllers DC power supply turned on and 3) system servoing inside MRI board. Three slices were acquired per imaging protocol for each configuration.

Compatibility was evaluated on a 3T Philips Achieva scanner. A 110 mm, fluid-filled spherical MR phantom was placed in the isocenter and the robot placed such that the tip was at a distance of 120 mm from the center of the phantom (a representative depth from perineum to prostate), as shown in Fig. 4(right). For the pneumatic robot, the phantom was imaged using four standard prostate imaging



**Table 1.** Scan Parameters for Compatibility Evaluation – 3T Philips Achieva

Protocol	FOV	TE	TR	Flip Ang	Bandwidth
<b>T1W</b>	240 mm	2.3 ms	225 ms	75°	751 Hz/pixel
<b>T2W</b>	240 mm	90 ms	3000 ms	90°	158 Hz/pixel
<b>FGRE</b>	240 mm	2.1 ms	6.4 ms	50°	217 Hz/pixel
<b>EPI</b>	240 mm	45 ms	188 ms	90°	745 Hz/pixel

protocols: 1) T1W FFE: T1 weighted fast field gradient echo; 2) T2W TSE: T2 weighted turbo spin echo; 3) TFE (FGRE): “real-time” turbo field gradient echo.

A baseline scan with each sequence was taken of the phantom with no robot components using round flex coils similar to those often used in prostate imaging. The following imaging series were taken in each of the following configurations: 1) phantom only; 2) controller in room and powered; 3) robot placed in scanner bore; 4) robot electrically connected to controller; and 5) robot moving during imaging (only with T1W imaging). For each step, all three imaging sequences were performed and both magnitude and phase images were collected.

The amount of degradation of SNR was used as the measure of negative effects on image quality. SNR of the MR images was defined as the mean signal in a 25 mm square at the center of the homogeneous sphere divided by the standard deviation of the signal in that same region. The SNR was normalized by the value for the baseline image, thus limiting any bias in choice of calculation technique or location. SNR was evaluated at seven 3 mm thick slices (representing a 25 mm cube) at the center of the sphere for each of the three imaging sequences. When the robot was operational, the reduction in SNR of the cube at the phantom’s center for these pulse sequences was 5.5% for T1W FFE, 4.2% for T2W TSE, and 1.1% for TFE (FGRE). Further qualitative means of evaluating the effect of the robot on image quality are obtained by examining prostate images taken both with and without the presence of the robot. Fig. 12 shows images of the prostate of a volunteer placed in the scanner bore on the leg rest. With the robot operational, there is no visually identifiable loss in image quality of the prostate.

## 6.2 MR Compatibility of Pneumatic Actuated Needle Placement Robot

As can be seen in Fig. 12, the motors and encoders provide very small visually identifiable interference with the operation of the scanner. Fig. 14 depicts one slice of the tracking fiducial frame which provides the full position information of the robot. We utilize SNR as the metric for evaluating MR compatibility with baseline phantom image comparison. For comparison, the SNR of each configuration was normalized by the average SNR of the 3 baseline images for each imaging protocol. SNR of the MR images is defined as the mean signal in a 25mm square at the center of the homogeneous sphere divided by the standard deviation of the signal in that same region [38]. The SNR was normalized by the value for the baseline image; thus limiting any bias in choice of calculation technique or location. The technique used for measuring SNR is equivalent to that described by the NEMA standard [2]. The SNR is calculated as described in Method 4 of the cited standard:

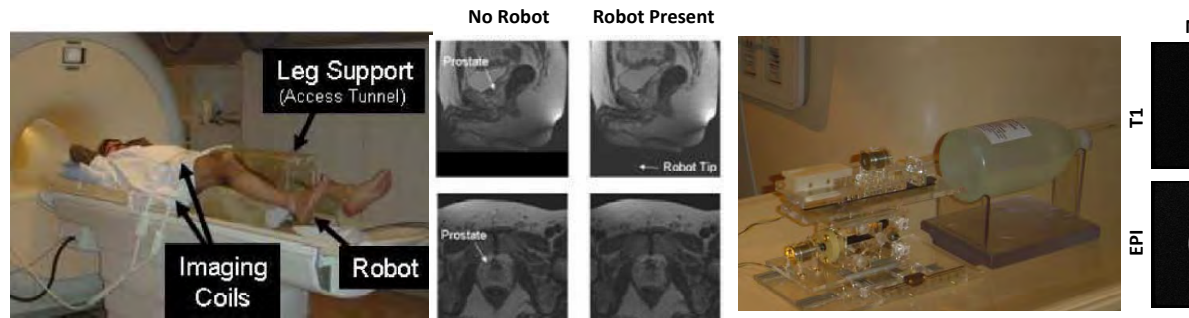


**Fig. 12.** Qualitative analysis of prostate image quality for pneumatic robot. Patient is placed on the leg support and the pneumatic robot sits inside of the support tunnel inside the scanner bore. T2 weighted sagittal and transverse images of the prostate taken when no robot components were present and when the robot was active in the scanner.

$$SNR = \frac{S}{imagenoise} \quad (1)$$

where,  $S$  is the mean pixel value within the Measurement Region of Interest (MROI) and  $imagenoise$  is the standard deviation (SD) of the selected Noise Measurement Region of Interest (NMROI). The location of the NMROI has a significant impact on calculated SNR; the selected NMROI in the top-left corner minimizes variance between image slices and is outside of ghosting artifacts as described by Firbank, *et al* [12]. Statistical analysis with a Tukey Multiple Comparison confirms that no pair shows significant signal degradation with a 95% confidence interval.

### 6.3 Accuracy of Pneumatic Actuated Needle Placement Robot

Accuracy assessment is broken into two parts: localization and placement. These two must be distinguished, especially in many medical applications. In prostate biopsy, it is essential to know exactly where a biopsy comes from in order to be able to form a treatment plan if cancer is located. In brachytherapy treatment, radioactive seed placement plans must be made to avoid cold spots where irradiation is insufficient; by knowing where seeds are placed, the dosimetry and treatment plan can be interactively updated. Based on encoder resolution, localization accuracy of the robot in free space is better than 0.1mm in all directions.

Positioning accuracy is dependent on the servo pneumatic control system. The current control algorithm for pneumatic servo control is based upon sliding mode control techniques. The pneumatic cylinder was commanded to move back and forth between two points and the steady state error for each move was recorded. The average positioning accuracy was 0.26mm RMS error. In addition to point-to-point moves, the positioning accuracy of the cylinder alone in free space has been evaluated for dynamic trajectory tracking. The cylinder was commanded to follow a 0.125Hz, 20mm amplitude sine wave. Fig. 13 shows the tracking results for the cylinder.

zero; as shown in Fig. 3.17, there is a lag in the valve response when pressure increases

from zero. A differential pressure between the cylinder sides based about a nominal pres-

sure greater than zero could eliminate this problem, but nonuniform valve responses made

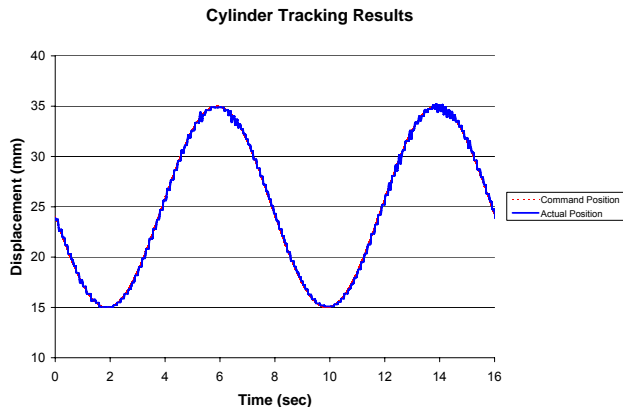


**Fig. 13** Dynamic tracking results for the pneumatic cylinder for an 8sec period, 20mm amplitude sine wave.

The RMS error for this task was 0.23mm which approximates the set deadband of 0.30mm.

### 3.7.2.2 Robotic System Accuracy

## 6.4 MR Compatibility of Piezoelectric Actuated Needle Placement Robot

As shown in Section 3.4.5, the kinematics for the robot are not linearly related to cylinder position. Therefore, the accuracy results in the previous section do not directly translate into the accuracy of the robot. In particular, the robot is inherently more accurate at the upper limits of its travel due to both the encoder resolution corresponding to motions in the scanner. The positioning accuracy of the robot was evaluated in the same setup and the same metric (SNR). As can be seen in Fig. 14 (left), the motors and encoders provide very small visually identifiable interference with the operation of the scanner. Fig. 14 (right) depicts one slice of the tracking fiducial frame which provides the full position information of the robot. Statistical analysis with a Tukey Multiple Comparison confirms that no pair shows significant signal degradation with a 95% confidence interval. This result presents significant improvement over recent research result in [20]. It implies that piezoelectric actuation is also feasible inside scanner bore during imaging, and thus makes it a good candidate in robotic design.

## 7 Discussion

This chapter presents two MRI-compatible approaches to image-guided transperineal prostate needle placement. Described is the robotic mechanism, actuator and sensor design, controller design and system integration for a pneumatically actuated robotic needle guide and a piezoelectrically actuated needle steering platform. The 2-DOF pneumatic robot with manual needle insertion has a SNR loss limited to 5% with alignment accuracy under servo pneumatic control better than 0.94mm per axis. While the 6-DOF piezoelectrically actuated robot is the first demonstration of a novel multi piezoelectric actuator drive with less than 2% SNR loss for high field MRI operating at full speed during imaging. The preliminary experiments in

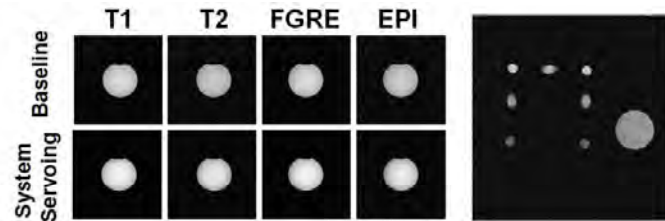


**Fig. 14.** Representative results showing the images obtained of baseline and system servoing inside scanner bore conditions (left), one slice of tracking fiducial frame besides a phantom. This result presents significant improvement over recent research result in [20](right).

phantom studies evaluates system MRI compatibility, workflow, visualization and targeting accuracy.

Attaining an acceptable level of MR compatibility required significant experimental evaluation. Several types of actuators, including piezoelectric motors and pneumatic cylinder/valve pairs, were evaluated. Pneumatic actuators have great potential for MRI-compatible mechatronic systems. Since no electronics are required, they are fundamentally compatible with the MR environment. However, there are several obstacles to overcome. These include: 1) material compatibility that was overcome with custom air cylinders made of glass with graphite pistons; 2) lack of stiffness or instability that was overcome with the development of a pneumatic brake that locks the cylinder's rod during needle insertion; and 3) difficult control that was ameliorated by using high-speed valves and shortening pneumatic hose lengths by designing an MRI-compatible controller. Pneumatic actuation seems to be an ideal solution for this robotic system, and it allows the robot to meet all of the design requirements. Further, MR compatibility of the system including the robot and controller is excellent with no more than a 5% loss in average SNR with the robot operational.

The pneumatic and piezoelectric systems have been evaluated in a variety of tests. The MR compatibility has shown to be sufficient for anatomical imaging using traditional prostate imaging sequences. Communications between all of the elements, including the robot, the low level controller, the planning workstation, and the MR scanner real-time imaging interface, are in place. Initial phantom studies validated the workflow and the ability to accurately localize the robot and target a lesion.

The pneumatic actuation and piezoelectric actuation presents complementary advantages and disadvantages. Pneumatic actuation is considered as the "ultimate solution" for MRI applications in the sense that these system can completely get rid of electrical and magnetic fields by using dielectric materials. However, due to the promising result implemented in the piezoelectric robot and the scalability, simplicity, size and inherent robustness of electromechanical systems present a clear advantage over pneumatically actuated systems. The piezoelectric actuation is considered as the rule of thumb actuation method that has been implemented as the slave robot presented here. A future development would be augmenting the slave

robot to a teleoperated master-slave system. The slave robot would perform the needle placement under the surgeon motion command while the needle insertion force would be measured using the fiber optic force sensors that are being developed [29–31].

## 8 Acknowledgements

This work is supported in part by the Congressionally Directed Medical Research Programs Prostate Cancer Research Program (CDMRP PCRP) New Investigator Award W81XWH-09-1-0191 and Worcester Polytechnic Institute internal funds. We are also grateful for the generous sample support from Igus, Inc.(Providence, RI).

## References

1. Standard test method for measurement of magnetically induced displacement force on passive implants in the magnetic resonance environment, F2052, vol. 13.01. American Society for Testing and Materials (ASTM) (2002)
2. Determination of Signal-to-Noise Ratio (SNR) in Diagnostic Magnetic Resonance Imaging, NEMA Standard Publication MS 1-2008. The Association of Electrical and Medical Imaging Equipment Manufacturers (2008)
3. Beyersdorff, D., Winkel, A., Hamm, B., Lenk, S., Loening, S.A., Taupitz, M.: Mr imaging-guided prostate biopsy with a closed mr unit at 1.5 t: initial results. *Radiology* **234**(2), 576–581 (2005). URL <http://dx.doi.org/10.1148/radiol.2342031887>
4. Blumenfeld, P., Hata, N., Dimaio, S., Zou, K., Haker, S., Fichtinger, G., Tempany, C.: Transperineal prostate biopsy under magnetic resonance image guidance: A needle placement accuracy study **26**(3), 688–694 (2007)
5. Bone, G., Ning, S.: Experimental comparison of position tracking control algorithms for pneumatic cylinder actuators. *IEEE/ASME Transactions on Mechatronics* **12**(5), 557–561 (2007)
6. Cavusoglu, M.C., Sherman, A., Tendick, F.: Design of bilateral teleoperation controllers for haptic exploration and telemanipulation of soft environments. *IEEE Transactions on Robotics and Automation* **18**(4), 641 – 647 (2002)
7. Chinzei, K., Miller, K.: Towards mri guided surgical manipulator. *Med Sci Monit* **7**(1), 153–163 (2001)
8. D’Amico, A.V., Cormack, R., Tempany, C.M., Kumar, S., Topulos, G., Kooy, H.M., Coleman, C.N.: Real-time magnetic resonance image-guided interstitial brachytherapy in the treatment of select patients with clinically localized prostate cancer. *Int J Radiat Oncol Biol Phys* **42**(3), 507–515 (1998)
9. DiMaio, S.P., Pieper, S., Chinzei, K., Hata, N., Haker, S.J., Kacher, D.F., Fichtinger, G., Tempany, C.M., Kikinis, R.: Robot-assisted needle placement in open MRI: system architecture, integration and validation. *Comput Aided Surg* **12**(1), 15–24 (2007)
10. Elhawary, H., Zivanovic, A., Davies, B., Lamperth, M.: A review of magnetic resonance imaging compatible manipulators in surgery. *Proc Inst Mech Eng [H]* **220**(3), 413–424 (2006)

24 Hao Su, Gregory A. Cole and Gregory S. Fischer

11. Elhawary, H., Zivanovic, A., Rea, M., Davies, B., Besant, C., McRobbie, D., de Souza, N., Young, I., Lamperth, M.: The Feasibility of MR-Image Guided Prostate Biopsy Using Piezoceramic Motors Inside or Near to the Magnet Isocentre. In: R. Larsen, M. Nielsen, J. Sporring (eds.) *Medical Image Computing and Computer-Assisted Intervention MICCAI 2006, Lecture Notes in Computer Science*, vol. 4190, pp. 519–526. Springer Berlin Heidelberg
12. Firbank, M.J., Coulthard, A., Harrison, R.M., Williams, E.D.: A comparison of two methods for measuring the signal to noise ratio on mr images. *Phys Med Biol* **44**(12), N261–N264 (1999)
13. Fischer, G.S., Iordachita, I.I., Csoma, C., Tokuda, J., DiMaio, S.P., Tempany, C.M., Hata, N., Fichtinger, G.: MRI-Compatible pneumatic robot for transperineal prostate needle placement. *IEEE/ASME Transactions on Mechatronics* **13**(3) (2008)
14. Fu, L., Liu, H., Ng, W.S., Rubens, D., Strang, J., Messing, E., Yu, Y.: Hybrid dosimetry: feasibility of mixing angulated and parallel needles in planning prostate brachytherapy. *Med Phys* **33**(5), 1192–1198 (2006)
15. Gassert, R., Dovat, L., Lamercy, O., Ruffieux, Y., Chapuis, D., Ganesh, G., Burdet, E., Bleuler, H.: A 2-dof fMRI compatible haptic interface to investigate the neural control of arm movements. *Proceedings. 2006 Conference on International Robotics and Automation*, pp. 3825–31. IEEE, Piscataway, NJ, USA (2006)
16. Gassert, R., Yamamoto, A., Chapuis, D., Dovat, L., Bleuler, H., Burdet, E.: Actuation Methods for Applications in MR Environments. *Concepts in Magnetic Resonance Part B: Magnetic Resonance Engineering* **29B**(4), 191–209 (2006)
17. Goldenberg, A., Trachtenberg, J., Kucharczyk, W., Yi, Y., Haider, M., Ma, L., Weersink, R., Raoufi, C.: Robotic system for closed-bore mri-guided prostatic interventions. *Mechatronics, IEEE/ASME Transactions on* **13**(3), 374 –379 (2008)
18. Haker, S.J., Mulkern, R.V., Roebuck, J.R., Barnes, A.S., Dimaio, S., Hata, N., Tempany, C.M.: Magnetic resonance-guided prostate interventions. *Top Magn Reson Imaging* **16**(5), 355–368 (2005)
19. Jemal, A., Siegel, R., Ward, E., Hao, Y., Xu, J., Thun, M.J.: Cancer statistics, 2009. *CA Cancer J Clin* **59**(4), 225–249 (2009)
20. Krieger, A., Iordachita, I., Song, S.E., Cho, N., Guion, P., Fichtinger, G., Whitcomb, L.: Development and preliminary evaluation of an actuated MRI-compatible robotic device for MRI-guided prostate intervention. In: *Robotics and Automation (ICRA), 2010 IEEE International Conference on*, pp. 1066 – 1073 (2010)
21. Krieger, A., Susil, R.C., Meard, C., Coleman, J.A., Fichtinger, G., Atalar, E., Whitcomb, L.L.: Design of a novel MRI compatible manipulator for image guided prostate interventions. *IEEE Trans Biomed Eng* **52**(2), 306–313 (2005)
22. Masamune, K., Kobayashi, E., Masutani, Y., Suzuki, M., Dohi, T., Iseki, H., Takakura, K.: Development of an MRI-compatible needle insertion manipulator for stereotactic neurosurgery. *J Image Guid Surg* **1**(4), 242–248 (1995)
23. Melzer, A., Gutmann, B., Remmele, T., Wolf, R., Lukoscheck, A., Bock, M., Bardenheuer, H., Fischer, H.: Innomotion for percutaneous image-guided interventions. *Engineering in Medicine and Biology Magazine, IEEE* **27**(3), 66 –73 (2008)
24. Mewes, P., Tokuda, J., DiMaio, S.P., Fischer, G.S., Csoma, C., Gobi, D.G., Tempany, C., Fichtinger, G., Hata, N.: An integrated MRI and robot control

- software system for an MR-compatible robot in prostate intervention. In: IEEE ICRA (2008)
25. Shellock, F.G.: Magnetic resonance safety update 2002: implants and devices. *J Magn Reson Imaging* **16**(5), 485–496 (2002)
  26. Song, S.E., Cho, N.B., Fischer, G., Hata, N., Tempny, C., Fichtinger, G., Iordachita, I.: Development of a pneumatic robot for MRI-guided transperineal prostate biopsy and brachytherapy: New approaches. In: Proc. IEEE International Conference on Robotics and Automation ICRA (2010)
  27. Spiczak, J.V., Samset, E., Dimaio, S., Reitmayr, G., Schmalstieg, D., Burghart, C., Kikinis, R.: Device connectivity for image-guided medical applications. *Stud Health Technol Inform* **125**, 482–484 (2007)
  28. Stoianovici, D., Patriciu, A., Petrisor, D., Mazilu, D., Kavoussi, L.: A new type of motor: pneumatic step motor. *IEEE/ASME Transactions on Mechatronics* **12**(1), 98–106 (2007)
  29. Su, H., Camilo, A., Cole, G., Hata, N., Tempny, C., Fischer, G.: High-field MRI compatible needle placement robot for prostate interventions. In: Proceedings of MMVR18 (Medicine Meets Virtual Reality). Newport Beach, California, USA (2011)
  30. Su, H., Fischer, G.S.: A 3-axis optical force/torque sensor for prostate needle placement in magnetic resonance imaging environments. In: 2nd Annual IEEE International Conference on Technologies for Practical Robot Applications. IEEE, Boston, MA, USA (2009)
  31. Su, H., Shang, W., Cole, G., Harrington, K., Gregory, F.S.: Haptic system design for MRI-guided needle based prostate brachytherapy. *IEEE Haptics Symposium 2010*. IEEE, Boston, MA, USA (2010)
  32. Sutherland, G.R., Latour, I., Greer, A.D., Fielding, T., Feil, G., Newhook, P.: An image-guided magnetic resonance-compatible surgical robot. *Neurosurgery* **62**(2), 286–92; discussion 292–3 (2008)
  33. Suzuki, T., Liao, H., Kobayashi, E., Sakuma, I.: Ultrasonic motor driving method for emi-free image in mr image-guided surgical robotic system. In: Proc. IEEE/RSJ International Conference on Intelligent Robots and Systems IROS 2007, pp. 522–527 (2007)
  34. Terris, M.K., Wallen, E.M., Stamey, T.A.: Comparison of mid-lobe versus lateral systematic sextant biopsies in the detection of prostate cancer. *Urol Int* **59**(4), 239–242 (1997)
  35. Tokuda, J., Fischer, G.S., Csoma, C., DiMaio, S.P., Gobbi, D.G., Fichtinger, G., Tempny, C.M., Hata, N.: Software strategy for robotic transperineal prostate therapy in closed-bore MRI. *Int Conf Med Image Comput Comput Assist Interv* (2008)
  36. Tsekos, N.V., Khanicheh, A., Christoforou, E., Mavroidis, C.: Magnetic resonance-compatible robotic and mechatronics systems for image-guided interventions and rehabilitation: a review study. *Annu Rev Biomed Eng* **9**, 351–387 (2007)
  37. Wallner, K., Blasko, J., Dattoli, M.: *Prostate Brachytherapy Made Complicated*, 2nd Ed. SmartMedicine Press (2001)
  38. Wang, Y., Cole, G., Su, H., Pilitsis, J., Fischer, G.: MRI compatibility evaluation of a piezoelectric actuator system for a neural interventional robot. In: Annual Conference of IEEE Engineering in Medicine and Biology Society, pp. 6072–6075. Minneapolis, MN (2009)

- 26 Hao Su, Gregory A. Cole and Gregory S. Fischer
39. Wang, Y., Su, H., Harrington, K., Fischer, G.: Sliding mode control of piezo-electric valve regulated pneumatic actuator for MRI-compatible robotic intervention. In: ASME Dynamic Systems and Control Conference - DSCC 2010. Cambridge, Massachusetts, USA (2010)
  40. Webster R.J., I., Kim, J.S., Cowan, N., Chirikjian, G., Okamura, A.: Nonholonomic modeling of needle steering. *International Journal of Robotics Research* **25**(5-6), 509–25 (2006)



---

# Closed-Loop Actuated Surgical System Utilizing Real-Time *In-Situ* MRI Guidance

G.A. Cole<sup>1</sup>, K. Harrington<sup>1</sup>, H. Su<sup>1</sup>, A. Camilo<sup>1</sup>, J. Pilitsis<sup>2</sup> and G.S. Fischer<sup>1</sup>

<sup>1</sup> Automation and Interventional Medicine Laboratory, Worcester Polytechnic Institute, Worcester, MA, USA [gcole, gfischer]@wpi.edu

<sup>2</sup> University of Massachusetts Memorial Medical School, Worcester, MA, USA

**Abstract.** Direct magnetic resonance imaging (MRI) guidance during surgical intervention can provide many benefits; most significantly, interventional MRI could be used for planning, monitoring of tissue deformation, real-time visualization of manipulation, and confirmation of procedure success. Direct MR guidance has not yet taken hold because it is often confounded by a number of issues including MRI-compatibility of existing surgery equipment and patient access in the scanner bore. This paper presents a modular surgical system designed to facilitate the development of MRI-compatible intervention devices. Deep brain stimulation electrode placement and prostate brachytherapy seed placement robots represent two examples. Phantom and human imaging experiments validate the capability of delineating anatomical structures in 3T MRI during robot motion.

## 1 Introduction

Diagnostic magnetic resonance imaging is one of the most effective imaging modalities available to the medical professional for viewing internal soft tissue structures. The ability to use this modality for live guidance during surgical procedures would prove invaluable for targeting or manipulating internal structures that are difficult to reach for procedures including deep brain stimulation (DBS) and percutaneous prostatic intervention.

Robotic assistance for guiding instrument placement in MRI for neurosurgery began with Masamune, *et al.* [9] and Chinzei, *et al.* [2]. Various methods are utilized to create and control motion within an MRI environment, as was outlined by Fischer *et al.* [5]. The authors have evaluated both pneumatic [4] and piezoelectric approaches [3]. There is additional work being developed in the area of pneumatically actuated robotic devices such as the PneuStep [10]. While this and other pneumatic technology does have a very low level of image interference, the scalability, simplicity, size and inherent robustness of electromechanical systems present a clear advantage over pneumatically actuated systems. A recent piezoelectric approach to prostatic interventions is described by Krieger, *et al.* [8], but as with other published piezoelectric actuation schemes, this one causes unacceptable image quality loss under

2 G.A. Cole, K. Harrington, H. Su, A. Camilo, J. Pilitsis and G.S. Fischer

motion and must interleave motion with imaging. *While these devices and others in [1, 6] do not depict the entire state of the art, they do highlight the problem being addressed: the current inability to generate and control precision electromechanical motion during live high-field (greater than 1.5T) closed-bore MR imaging without affecting the quality of the image.* The main contributions being discussed in this paper are the system architecture for the rapid development of procedure-specific MRI-guided surgical intervention systems, two example implementations of this system architecture, and experimental validation of their functionality. The two representative procedures targeted are DBS lead placement and prostate brachytherapy.

## 2 Technical Approach

One of the greatest challenges to creating an MRI-guided robotic system is achieving the required MRI compatibility in terms of safety and image quality [5]. While there are many safety concerns with MRI compatibility in terms of magnetic and conductive materials, employing material restrictions during the design process can easily and effectively minimize these risks. It has been shown that a much more difficult to control compatibility issue is image interference [8, 2]. Most common forms of electronics, especially those containing oscillators, will generate noise in the MR image that will reduce the quality of the images, sometimes to the point that they will not be useful for therapeutic medicine.

Avoiding the high frequency electrical noise problems are very difficult when constructing an MRI compatible system with active motion. A major difficulty in the proposition of constructing an MRI compatible actively driven system is that there are very few “off-the-shelf” products that can be used in the sensitive magnetic environment without destroying the quality of images. The focus of this research is to develop a series of modules that will allow the rapid creation of MR compatible actively driven systems.

### 2.1 System Architecture

The components of the system presented are specifically constructed for use within an MR scanner and the system is designed to be modular and highly expandable to accommodate a wide variety of needs. As shown in Fig. 1, the architecture is constructed of three primary components that are independent of the hospital equipment: user workstation, controller, and robotic mechanism. The user workstation (typically a laptop computer) resides in the MRI console room, while the robot controller is in the scanner room and the robotic device operates in the MRI scanner bore. The system is completely portable and not coupled to the scanner room – the only external connections are a fiber optic cable that passes through the waveguide and AC power from the wall sockets in the MRI scanner room.

The user workstation resides in the MRI console room and acts as the primary planning and navigation software interface. The system architecture supports a variety of surgical planning platforms by supporting the OpenIGTLink communication protocol between the workstation and the controller [14]. Using the Slicer navigation software platform as described in [13], MR images are compounded into a three dimensional model which is used for procedure planning and interactive guidance

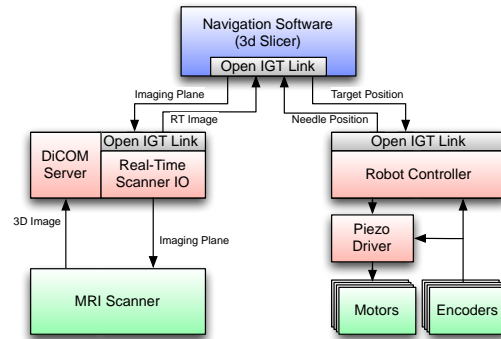


**Fig. 1.** Architecture of the modular MRI-compatible surgical system.

tracking. The workstation communicates with the hospital imaging equipment and is responsible for acquiring the MR images and optionally controlling the scanner.

The navigation software sends target and motion commands to the in-room robot controller, which sends back pose and trajectory information about the robotic mechanism. As configured, the navigation software need not know the robot kinematics – all commands are passed between the planning workstation and robot controller in patient (i.e. RAS) coordinates. The controller itself houses a majority of the original modules: motor drivers, backplane, power supplies, Faraday cage, and control computer. Typically the control computer within the controller contains kinematic information about the mechanism within the scanner bore, and interprets pose commands from the user workstation into joint commands for the mechanism. It then sends these position or velocity commands to the motor drivers, via the backplane. The drivers then produce power signals to operate actuators in the mechanism, and receives and analyzes encoder information for the corresponding degrees of freedom. Through this system architecture, a varying plurality of degrees of freedom can easily and quickly be integrated into a single system. To increase modularity, the backplane has an ethernet interface that can be directly coupled to the fiber optic media converter (as opposed to the internal embedded control computer) to alternatively allow the higher level kinematic control to be performed on a computer outside the scanner room.

## 2.2 System Modules

All of the presented original system modules were developed because the authors did not feel that any commercial off-the-shelf (COTS) item would accomplish the desired task without causing signal degradation in the scanner images. One of the more common methods for creating actuated motion in an MRI is the use of piezoelectric actuators due to their inherent non-magnetic mode of operation, and the high degree of precision achievable by the actuators. Unfortunately, the available drivers used to operate these motors, while generally not causing interference by their presence in the scanner, do tend to cause a large amount of image degradation while the motors they drive are being driven [7, 5]. The following describes the specific custom components of the modular MRI-compatible robotic system, with an example system configuration shown in Fig. 2.

4 G.A. Cole, K. Harrington, H. Su, A. Camilo, J. Pilitsis and G.S. Fischer

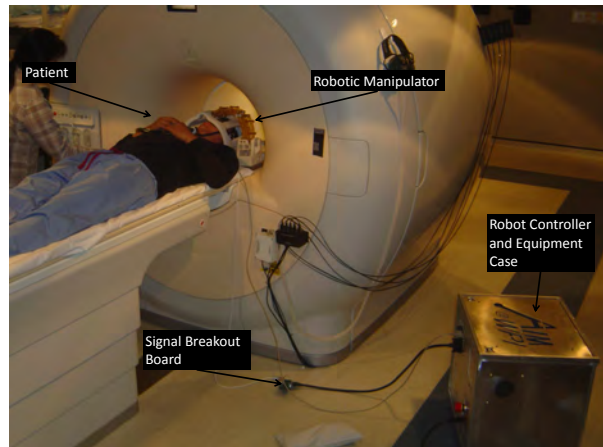


**Fig. 2.** Example configuration of the robotic system with the controller and other equipment within the scanner room.

*Piezoelectric Actuator Driver* The primary objective during the design of this device was to create a generalized controller that could operate a multitude of piezoelectric actuators. There are many shapes and forms of piezoelectric actuators, and they generally fall into two major categories: harmonic and non-harmonic. Harmonic motors, also known as ultrasonic motors, often operate at higher speed and lower torque than non-harmonic motors, and utilize high voltage (200-300 volt) driving waveforms at high frequency (30-50kHz). Some examples of these motors are the Shinsei ultrasonic motor as described in [2], and the Nanomotion HR series of motors described in [8]. While typically the drivers created for these motors output simple sine waves, it was desired to have the ability to finely control the shape of the output waveform to optimize mechanical performance and MR compatibility. In order to accommodate the fine tuning of motor performance, the piezoelectric driver board was constructed with an FPGA-based very high speed (12 mega-samples per second per channel) arbitrary waveform generator, coupled to a high current linear output stage, which is operated with a separate independent power rail. The high degree of precision allows the user to control high frequency signal components being passed through the output stage, which could otherwise be expressed as noise or artifacts in scanner images.

While non-harmonic motors, operate at a much lower frequency than harmonic motors (750Hz to 3kHz) they require a high precision non-sinusoidal waveform to be operated most effectively. Examples of these waveforms are shown in Fig. 3. Because the shape of the driving waveforms for non-harmonic motors is not a sinusoidal wave, the wave can naturally be broken down into much higher frequency components. Due to the possibility of these components generating noise in scanner images, precision control of these waveforms is coupled with low-pass filtering on the output. Combining this high speed arbitrary waveform generator and high current output stage with a microprocessor capable of communicating via USB or through the Ethernet backplane allows these driving units to be rapidly integrated into a functional controller. This unit took on the form shown in Fig. 4.

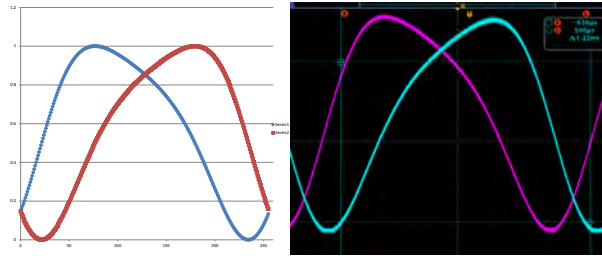


**Fig. 3.** Example waveform for non-harmonic motors with desired input (left) and output from piezo driver board (right). The driver outputs this 2000 point waveform at up to 3kHz

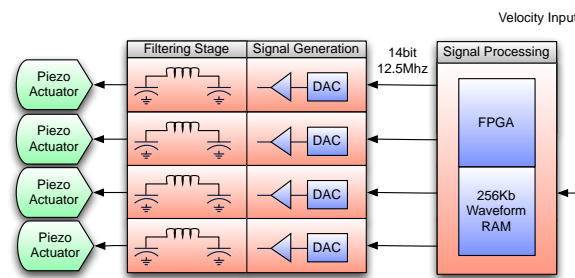


**Fig. 4.** Configuration of the generalized MR-compatible piezoelectric driver board. The board performs all low-level control and waveform generation and drives up to four piezo elements in a single or multiple motors.

As can be seen from the diagram, the signal processing stage receives an input in the form of a velocity or position setpoint. This signal processing block can then create four independent channels of driving waveforms with a data rate of 12.5 mega samples per second (MSPS) of 14 bit resolution. The signal generators include a high power output amplification stage, which passes its signals out to the actuators through a  $\pi$  filter. The boards also integrate position encoding (from differential encoder receivers) such that closed-loop motion control loops can take place within the FPGA, distributing the real-time processing of the system.

*Backplane Signal Aggregator* As has been referenced earlier, a plurality of motor drivers are used for each of the configurations implemented with the system architecture. The software structure of the system uses a single server to interface between the piezoelectric driver boards and the control computer. A PIC microcontroller ethernet device concatenates the lines of communication to and from the controller computer and the driver boards, utilizing a communication protocol known as the Bowler Communication System. This structure is expressed through a backplane connector containing a series of board edge connectors to plug drivers into, an ethernet board connector, and output connectors for shielded cables. Multiple configurations of the backplane can be customized for the requirements of the particular application. The current system is based on a 10-port backplane with two 68-pin shielded, twisted pair VHDCI cables connecting differential encoder lines and motor power to a distribution block on the robot (5 axes each).

6 G.A. Cole, K. Harrington, H. Su, A. Camilo, J. Pilitsis and G.S. Fischer

*Power Supply* A significant source of noise when attempting to operate electrical equipment within an MR scanner room can be switching power converters supplies. One theory is this noise is caused by the high frequency operation, generally on the order of (150kHz to 600kHz) of switching regulators, coupled with their rejection of noise both on the input and the output of the regulators. Because of this, many developers of MR compatible technologies utilize linear regulators (which are highly inefficient), or power supplies external to the scanner room to create DC voltages that are then passed through the patch panel to supply the in-room equipment (which requires scanner-specific connections and an additional source of noise infiltration). In the proposed architecture, a medical grade linear AC-DC converter generated 48 VDC from the in-room AC supply. To create a power supply that would be capable of operating with a high degree of efficiency (over 85%) while still maintaining MRI compatibility, a switching regulator was designed to operate at a switching frequency of approximately 15kHz, while still maintaining an output ripple voltage under 5 mV. In addition to this, over 15,000 uF of input capacitance was implemented in order to minimize noise that could be rejected on the input to the power supply. The design of this power supply was extensively simulated under varying loading conditions to ensure that it would operate effectively under changing conditions, such as motors switching on and off, or varying computational loads.

*Control Computer* The control computer in the in-room controller box in general is expressed as a COTS small form factor computer, that has been modified to be powered off of the supply rails generated by the power supply stages. Previous versions of the controller have used the PC104 form factor, the latest version uses a mini-ITX computer. In general, with a grounded housing and continuous shielded case on a computer such as this, without the original noisy switching power supply, these computers can be operated within the equipment case without much scanner interference [15]. As described earlier, this computer interprets movement and target commands from the user workstation (using the OpenIGTLink) to joint and actuator commands through the use of kinematic information about the mechanism being utilized. In general, this computer communicates to the backplane through an Ethernet socket and to the user workstation through a fiber optic Ethernet connection. To allow a more distributed software architecture, the communication proxy server, trajectory generator, and kinematics engine can be separate applications that communicate over a local network socket. The fiber optic network connection between the control computer and user workstation is utilized to avoid passing any electrical signals through the patch panel which can lead to image interference.

*EMI Shielded Enclosure* As discussed before, signal integrity preservation is one of the main difficulties facing the creation of MR compatible robotic systems. A key step in reducing image degradation from electrical noise, is to encase all electronics in a continuous Faraday cage to block as much electromagnetic interference (EMI) being emitted from the equipment as possible. This cage is extended through the shielded cables carrying electrical signals out of the cage. This enclosure is designed to support the modular nature of the system architecture by combining an integrated base of support functionality such as power rail generation and fiber optic communication, with a reconfigurable equipment area as shown in Fig. 5. By making it easy to change out the equipment and system modules within this case, new devices can be integrated and tested streamlining the design process. After the

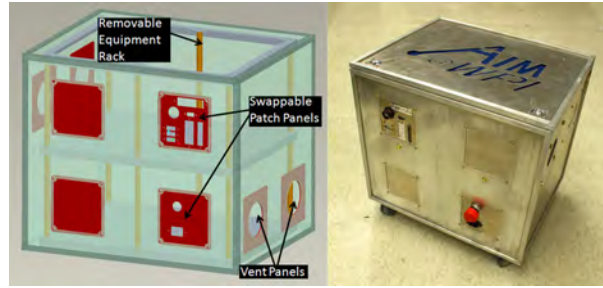


**Fig. 5.** Solid model of enclosure showing swappable patch panels to allow for different equipment configurations (left) and a photograph of manufactured case (right).

procedure-specific system is tested and verified as functional, a new controller, with dedicated devices can be assembled with a more compact construction.

*Tracking Fiducial* One of the challenges implementing image guided surgical procedures, is registering the robotic equipment with the image space. To accomplish dynamic global registration between the robot and the scanner, a passive tracking fiducial frame shown in Fig. 6 is implemented as described in [4]. This fiducial frame is constructed of ABS plastic with seven embedded MR Spot fiducials (Beekley, Bristol, CT). These embedded fiducials form a Z shape in three different planes as shown in 6. By utilizing this arrangement, any arbitrary MR image slicing through all of the rods can provide a full 6-DOF pose of the frame, and thus the robot, with respect to the scanner. By locating the fiducial attached to the robot, the transformation between patient coordinates and the robot's needle driver is known. By transmitting the fiducial's coordinate frame to the robot controller, the end effector location is then calculated from the kinematics based on encoder positions.

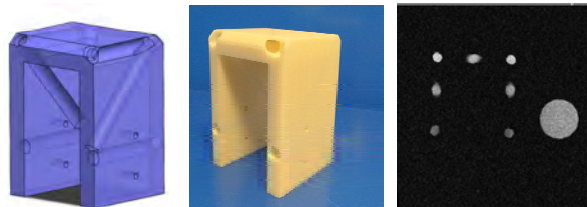


**Fig. 6.** Left: Solid model of tracking fiducial frame, Middle: tracking fiducial frame used in experiment, Right: Once tracking fiducial frame beside a phantom.

*Motion Platform* In general, each mechanism is specifically created for a given procedure. Typically a prismatic mechanism is required when placing the base point of that mechanism to an appropriate location in image space with reference to the patient. Because of the expected repeated necessity for an X-Y-Z type translation to locate a procedure-specific mechanism to a desired base point with reference to a patient, a 3-axis translational stage was developed as a system module. The X-Y-Z stage is a compact form factor design, with the two perpendicular horizontal degrees

8 G.A. Cole, K. Harrington, H. Su, A. Camilo, J. Pilitsis and G.S. Fischer

of freedom being actuated by linear piezoelectric motors, and the vertical stage, due to the much higher forces expected to be required, being actuated by a scissor-lift connected rotary motor. This is one example of a base for the application-specific manipulator that can be customized for range of motion and spatial constraints as required.

### 3 Clinical Applications: Two Example Procedures

As a show of the systems modularity, two example interventional systems are being developed in parallel by our research group targeting two different procedures: prostate brachytherapy and DBS electrode placement. While these procedures are very different, because they are both performed on deep, hard to reach soft tissue structures, they could greatly benefit from MR guidance to improve performance and reduce trauma. Each application has a custom end effector mechanism that plugs into a common system architecture.



**Fig. 7.** Photograph of the remote center of motion (RCM) linkage portion of the DBS insertion mechanism that couple to the above-mentioned translational motion base.

#### 3.1 DBS Electrode Placement System

The most common target for DBS electrodes, the subthalamic nucleus (STN), is deep within the brain and therefore cannot be directly seen during the procedure. In order to accurately target the STN in a traditional procedure, a lengthy registration procedure is required during which time the patient is under a considerable amount of motion. Coupled with the fact that the MR images utilized to create the surgical plan were taken before the cranium is punctured and some of the cerebrospinal fluid is removed, there is a clearly an opportunity for tissue shift and registration inaccuracy. In order to combat this registrational difficulty, micro electrode recordings are often used to verify correct electrode placement, though these recordings cannot be made with the DBS electrodes themselves. All of these factors can be reduced to the



same problem: there is no *live, in-situ confirmation of electrode location while the electrode is being placed*. Inaccurate placement of electrodes has been shown to cause side effects ranging from procedure ineffectiveness to new psychological symptoms and even death [3]. By giving the surgeon access to interactively updated MR imaging during a procedure, there is an opportunity for greater accuracy, in addition to greatly streamlining and shortening the procedure by bypassing complicated, multi modality registration procedures, and allowing the entire procedure to be performed with the patient remaining in one location. This reduces anesthesia usage, trauma and cost of the procedure as well. The equipment setup for this proposed system is shown in Fig. 7.

This system was constructed utilizing all of the standard modules listed above, with eight actuator drivers corresponding to the eight possible degrees of freedom (DOF). In addition to this, the mechanism was designed and constructed to be kinematically identical to the Leksell frame, the current standard for DBS electrode insertion, as shown in Fig. 7. By making the new mechanism kinematically equivalent to the currently used technology of the Leksell frame (a 5-DOF device), it is the authors hope to streamline the adoption of the new system into use by making the procedural planning very similar for the new and old systems. Initially, a 5-DOF system is targeted (three translational DOF, two rotational DOF), indicating a manual insertion, though eventually an 8-DOF system will be developed to integrate active insertion control, as well as providing an additional two degrees of rotation at the end effector to increase armature dexterity as seen in 7.

### 3.2 Prostate Needle Placement System

The needle placement mechanism utilizes the same types of actuators and encoders as the DBS system, thus an identical controller configuration is utilized. This needle placement mechanism, constructed primarily of rapid prototyped ABS plastic and laser cut acrylic, is comprised of two main segments, a 3-DOF needle driving module (insertion, cannula retraction, and needle rotation) and the generalized 3-DOF cartesian positioning module as described in [12, 11]. This system was designed to work in a configuration similar to TRUS-guided brachytherapy, and as such the MRI bore's 60 cm diameter constrains the spread of the legs and limited the width of the robot to 7 cm. The lower motion platform layer provides linear motion from embedded piezoelectric actuators, while the upper needle driver module layer provides cannula rotation and stylet prismatic motion. This structure minimizes the "between leg" space while the lower Cartesian stage takes advantage of the available "under leg" space.

## 4 Experimental Validation

*Phantom Test – Quantitative Study* To date there have been a series of experiments with this system, mainly focusing on the ability of the system to generate and control motion while remaining MR compatible. All of the modules presented earlier have been tested individually and as a whole, to ensure that no aspect of the system creates an unacceptable amount of image interference. The specific scan protocols are the same in [15]. The metric of choice to measure signal loss is signal

10 G.A. Cole, K. Harrington, H. Su, A. Camilo, J. Pilitsis and G.S. Fischer

**Table 1.** Experimental Results of MRI Compatibility Evaluation showing average SNR for each case and percent difference from baseline

Protocol	Baseline	Motor Off (%change)	Motor Running (%change)
T1W	148.7	150.5 (1.24%)	149.8 (0.76%)
T2W	620.4	631.8 (1.84%)	629.4 (1.46%)
FGRE	141.2	142.8 (1.19%)	141.6 (0.30%)
EPI	228.4	223.6 (2.09%)	226.3 (0.92%)

to noise ratio (SNR) which compares an image section that is expected to be 100% signal with an image section expected to be 100% dark, as can be seen in Fig. 8. The results of the total system demonstrate a very low amount of interference as ca

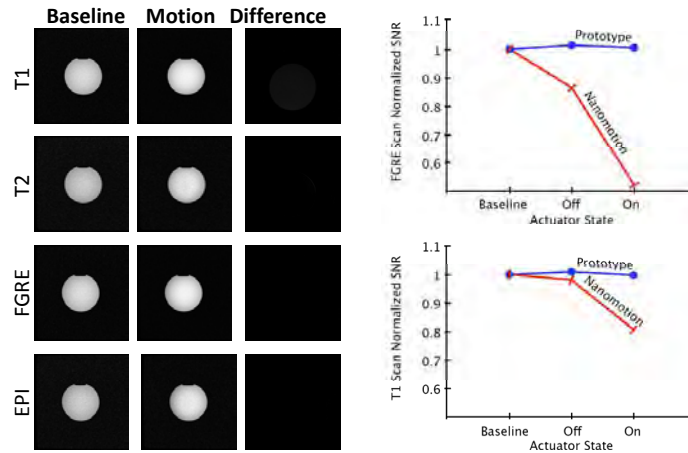


**Fig. 8.** Left: Image subtraction analysis of interference caused by equipment. Right: Plot of normalized SNR comparing prototype presented in this paper and the one in [8].

*Pre-Clinical Evaluation – Qualitative Study* In another series of tests performed, images of a living human subject’s brain were acquired during robot motion and shown to several radiologists; the images were determined to be indistinguishable from images taken without any equipment being present in the scanner room. A qualitative demonstration of an operating surgical system on image quality is shown in the anatomy image Fig. 9.

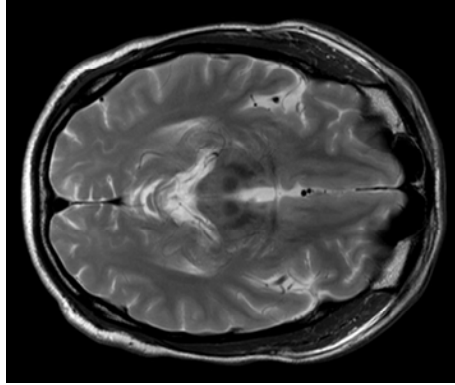


**Fig. 9.** Clear image of patient anatomy indicating usefulness of images for surgical planning. Note in the image, the lack of background noise.

## 5 Discussion

It has been shown that the modular surgical system is both capable of creating and controlling motion in an MR scanner without causing image interference, and that the system can be adapted to a multitude of procedure specific mechanisms. Physical performance of the system is to be thoroughly evaluated beginning with robot's precision and clinical ergonomics of the system's configuration. The first phase of this testing will be to determine that accuracy with which the system can move and control its degrees of freedom with reference to itself. The next phase of this testing will be to determine that accuracy with which the system can position itself with respect to image space. Once these performance areas are verified, the system will be tested for ergonomics and usability. After the final rounds of experimental validation discussed in the previous section is completed, these two systems will be moved into cadaver and clinical trials, while new modules and procedures to be incorporated into the modular device set will be pursued. MRI is a highly effective soft tissue imaging system, and the ability to utilize this procedure in-vivo coupled with precision computer controlled motion will prove to be an invaluable asset in the future development of minimally invasive surgery. The authors hope the presented modular robot controller system will help to expedite the the development of clinically viable MR image-guided robotic surgery systems.

*Acknowledgements* This work was funded in part by the Congressionally Directed Medical Research Programs Prostate Cancer Research Program New Investigator Award W81XWH- 09-1-0191 and Worcester Polytechnic Institute internal funds.

## References

1. Carpi, F., Khanicheh, A., Mavroidis, C., De Rossi, D.: MRI compatibility of silicone-made contractile dielectric elastomer actuators. *Mechatronics, IEEE/ASME Transactions on* **13**(3), 370–374 (2008)
2. Chinzei, K., Hata, N., Jolesz, F.A., Kikinis, R.: Surgical assist robot for the active navigation in the intraoperative MRI: hardware design issues **1**, 727–732 (2000)

- 12 G.A. Cole, K. Harrington, H. Su, A. Camilo, J. Pilitsis and G.S. Fischer
3. Cole, G., Pilitsis, J., Fischer, G.S.: Design of a robotic system for mri-guided deep brain stimulation electrode placement. In: Proc. IEEE Int. Conf. Robotics and Automation ICRA '09, pp. 4450–4456 (2009)
  4. Fischer, G.S., Iordachita, I., Csoma, C., Tokuda, J., DiMaio, S.P., Tempany, C.M., Hata, N., Fichtinger, G.: MRI-Compatible pneumatic robot for transperineal prostate needle placement. *IEEE/ASME Transactions on Mechatronics* **13**(3), 295–305 (2008)
  5. Fischer, G.S., Krieger, A., Iordachita, I., Csoma, C., Whitcomb, L.L., Fichtinger, G.: MRI compatibility of robot actuation techniques—a comparative study. *Med Image Comput Assist Interv* **11**(Pt 2), 509–517 (2008)
  6. Gassert, R., Moser, R., Burdet, E., Bleuler, H.: MRI/fMRI-compatible robotic system with force feedback for interaction with human motion. *Mechatronics, IEEE/ASME Transactions on* **11**(2), 216–224 (2006)
  7. Kokes, R., Lister, K., Gullapalli, R., Zhang, B., MacMillan, A., Richard, H., Desai, J.: Towards a teleoperated needle driver robot with haptic feedback for RFA of breast tumors under continuous MRI. *Medical Image Analysis* **13**(3), 445–55 (2009)
  8. Krieger, A., Iordachita, I., Song, S.E., Cho, N., Guion, P., Fichtinger, G., Whitcomb, L.: Development and preliminary evaluation of an actuated MRI-compatible robotic device for MRI-guided prostate intervention. In: *Robotics and Automation (ICRA), 2010 IEEE International Conference on*, pp. 1066–1073 (2010)
  9. Masamune, K., Kobayashi, E., Masutani, Y., Suzuki, M., Dohi, T., Iseki, H., Takakura, K.: Development of an MRI-compatible needle insertion manipulator for stereotactic neurosurgery. *J Image Guid Surg* **1**(4), 242–248 (1995)
  10. Stoianovici, D., Patriciu, A., Petrisor, D., Mazilu, D., Kavoussi, L.: A new type of motor: pneumatic step motor. *IEEE/ASME Transactions on Mechatronics* **12**(1), 98–106 (2007)
  11. Su, H., Camilo, A., Cole, G., Hata, N., Tempany, C., Fischer, G.: High-field MRI compatible needle placement robot for prostate interventions. In: *Proceedings of MMVR18 (Medicine Meets Virtual Reality)*. Newport Beach, California, USA (2011)
  12. Su, H., Shang, W., Cole, G., Harrington, K., Gregory, F.S.: Haptic system design for MRI-guided needle based prostate brachytherapy. In: *IEEE Haptics Symposium 2010*. IEEE, Boston, MA, USA (2010)
  13. Tokuda, J., Fischer, G.S., DiMaio, S.P., Gobbi, D.G., Csoma, C., Mewes, P.W., Fichtinger, G., Tempany, C.M., Hata, N.: Integrated navigation and control software system for MRI-guided robotic prostate interventions. *Comput Med Imaging Graph* **34**(1), 3–8 (2010)
  14. Tokuda, J., Fischer, G.S., Papademetris, X., Yaniv, Z., Ibanez, L., Cheng, P., Liu, H., Blevins, J., Arata, J., Golby, A.J., Kapur, T., Pieper, S., Burdette, E.C., Fichtinger, G., Tempany, C.M., Hata, N.: Openiglink: an open network protocol for image-guided therapy environment. *Int J Med Robot* **5**(4), 423–434 (2009)
  15. Wang, Y., Cole, G.A., Su, H., Pilitsis, J.G., Fischer, G.S.: MRI compatibility evaluation of a piezoelectric actuator system for a neural interventional robot. In: *Proc. Annual Int. Conf. of the IEEE Engineering in Medicine and Biology Society EMBC 2009*, pp. 6072–6075 (2009)